Abstract

MAGID, KAREN RUTH. Generation and Characterization of Micron and Sub-micron Sized Particulate using Electrothermal Plasma Source SIRENS. (Under the direction of Dr. Mohamed A. Bourham)

The **S**urface **I**nteraction **R**esearch **E**xperiment at **N**orth Carolina **S**tate (SIRENS) is an electrothermal plasma facility which was recently used to generate particulate for the enhancement and modification of surfaces. The modification of fabrics by surface coating or particle implantation was the main goal of this work. The SIRENS facility generates a low temperature, high density plasma using an exchangeable liner. The plasma expands from a 4mm diameter capillary into a 180mm diameter expansion cell inside a larger vacuum chamber where collection substrates and diagnostics can be used to collect particulate and analyze the plasma. A variety of conductive and nonconductive materials were used as both sources and substrates. Important for the surface modification applications is to analyze the particulate for composition and size from scanning electron microscope (SEM) images with particle counting software. Also important for the goal of eventually linking the plasma to the particulate generated is to characterize the plasma as it expands into the collection chamber. Therefore, the plasma density and temperature were measured using optical emission spectroscopy at distances 7, 32, 47, and 68cm from the source exit.

Shots were performed at similar input energies, approximately 5.7 ± 0.14kJ. Particulate was collected using aluminum, copper, mixed aluminum/copper, Lexan, and Teflon liners. The aluminum, copper, and mixed materials all produced significant amounts of particulate that was visible with an SEM on both metal and fabric substrates. The Lexan and Teflon liners produced particulate that was only visible on fabric substrates. Washing tests showed that some particulate remained on woven fabrics after repeated washings.

The SEM images were recorded and analyzed to determine the number and size of the particulate on a substrate. Based on observations of the countable particulate, the particles were approximated as spheres and sized by the diameter determined from the measured area. Particle size ranged in diameter from approximately 0.1μm to 3.5μm, with the average size falling at or slightly below 1μm in diameter. Important observations of aluminum particulate was that much melting occurred so that long streaks of solidified molten material were observed on the metal substrates. The size of the aluminum particles also showed a generally increasing trend with increasing distance from the source. The copper particles did not show the increasing trend and were, on average, smaller at each location. The mixed materials

test returned particles composed of both metals, and with average diameters between those of pure aluminum and copper. The Lexan and Teflon particulate on fabric was too difficult to count and size; however one sample exposed to Teflon was more hydrophobic than an unexposed sample of the same fabric.

The plasma was also analyzed for temperature and density using optical emission spectroscopy. The results obtained experimentally were also compared to estimations of the plasma parameters based on the electrical and mass difference measurements of the discharge. Using the relative line method to construct Boltzmann plots, the temperatures of aluminum, copper, and Lexan plasmas were determined to be 0.5 ± 0.125eV from the neutral copper lines. This temperature remained constant over the length of the discharge. The electron densities were determined from both Stark broadening of the H_α line and the neutral copper lines. The densities were found to be in the range of 10^{22}-10^{24} m^{-3}, with a more distinct decreasing trend with distance using the densities from the hydrogen line broadening. The parameter estimates from the discharge characteristics returned higher temperatures and lower densities. The estimates are useful for confirming the neutral-dominated and LTE assumptions about the plasma.

Generation and Characterization of Micron and Sub-micron Sized Particulate using Electrothermal Plasma Source SIRENS

by

Karen Ruth Magid

A thesis submitted to the Graduate Faculty of
North Carolina State University
in partial fulfillment of the
requirements for the Degree of
Master of Science

Nuclear Engineering

Raleigh, North Carolina

July 2003

Approved by:

Dr. Mohamed A. Bourham (chair)	Dr. John Gilligan
Dr. Mansoor Haider (minor)	Dr. John Blondin (minor)

Biography

Karen Magid was born in Detroit, Mi. on March 2, 1979, the second child of Jill Ray and Howard Magid. She moved to Raleigh, NC in 1981 where she stayed except for one year in Nice, France until she graduated from Ravenscroft School in June of 1997. In August of that year, she enrolled at Northwestern University in the McCormick School of Engineering, until she transferred to North Carolina State University in December of 1999. She graduated with a Bachelor of Science in Electrical Engineering in December of 2000. After briefly working as a hardware engineer at Lucent Technologies, she began her graduate study in Plasma Science at N. C. State University in the department of Nuclear Engineering.

Acknowledgements

I would like to acknowledge the time and efforts of my committee members Drs. Bourham, Gilligan, Haider, and Blondin. Numerous discussions were had about the research as well as the first drafts of this work. Talking with each never failed to help clarify my own thoughts and provide me confidence in my understanding of and ability in the work. Additionally, I must acknowledge Dr. Phil Sharpe, upon whose work much of this work is based. He generously answered the questions that got me started on the right track.

I also have to thank Mr. Mark Barefoot for his many hours spent helping me in the lab. I probably over used his expertise, which he generously offered. He helped me with everything from minor circuit problems to unsolvable circuit problems. Similarly, Larry DuFour and the Precision Machine Shop were indispensable with their time and expertise.

My colleagues were also very helpful. They provided a sounding board for many ideas and hours of discussion about our research. They were also usually available when sudden problems arose in the course of an experiment. These were my fellow plasma guys Travis Gray, Brian Bures, and Jason Haverkamp. In addition, Suzanne Rodden helped me with any fabric questions and generously performed all washing tests.

I would also like to acknowledge the support of the National Textile Center, contract #M02-S09, and partial support from the Office of Naval Research N00014-02-1-0868.

Contents

List of Figures

List of Tables

Chapter 1

Introduction

1.1 Electrothermal Plasma Sources

Electrothermal plasma sources are capable of creating high density ($10^{13} - 10^{16}$ cm^{-3}) and low temperature (1 - 3 eV) plasmas. Traditionally, electrothermal plasma guns have been studied for use mainly in electrothermal-chemical (ETC) and plasma-material interaction applications including plasma propellant interactions [1], fusion studies [2], and other defense applications [3], [4], and [5].

The **S**urface **I**nteraction **R**esearch **E**xperiment at **N**orth Carolina **S**tate, SIRENS, is an electrothermal plasma source which was developed in 1987 to examine high-heat flux plasma-material interactions. The plasma is initiated in the device by a capillary-arc discharge and produced by the ablation of the capillary liner material. The liner material can be made of any machineable material.

In the past, this facility has been used almost exclusively for electrothermal applications such as electrothermal-chemical guns and electromagnetic launchers. These applications tended to focus on the plasma generated by the pulsed capillary discharge and the modelling of the source. For example, the ablation from the discharge has been examined in SIRENS and other similar devices, in studies such as [6] and [7]. The plasma has been modelled for the purpose of optimizing the performance of ETC guns in [4] and [3]. Recently, however, the device has been applied to different surface modification application. Of particular interest is the modification of textiles by implantation of coating. One specific application is the possibility of conductive fabrics or a conductive pattern implanted into an article of clothing which could be used as antennas or very light-weight wiring. A more traditional application for modified fabric is increasing the resistance to water by making a fabric more hydrophobic. If a fabric is more resistant to absorbing water, then it can last longer in situations such as conveyor belt.

1.2 Micro and Nano Particulate Generation

The surface modification technique implemented with an ET plasma source involves the generation of small particulate. The pulsed capillary discharge is an ablative process. The ablation of the liner material produces a plasma jet that rapidly expands and cools outside the capillary. Though the ET plasma is a high density plasma, it is dominated by neutral species and can contain molten material. Substrates placed in the path of the expanding jet can capture this material in the plasma jet. The material is in the form of small particulate.

While particulate generation has not been one of the traditional focuses for research on electrothermal devices, there have been a few previous studies which looked into the particulate generated from this type of discharge. Several studies have looked at particulate for fusion research, because characterizing the dust is important for safety limits. The SIRENS device was used in [8] and [2] as a way to simulate tokamak disruption heat loads and the particulate generated by such an event. While the application of the particulate generated in this work was different than the present work, the review of particulate generation methods therein are useful. Other studies, such as [9], have looked at particulate generation via pulsed capillary discharge for the purpose of coatings, or surface modification. Another study, [10], looked at nanoparticle generation with an electrothermal-chemical gun for the basic study of materials synthesis and for the possibility of new semiconductors.

Besides the research into its generation, particulate characterization has been the focus of much microscopy research. Automation of the counting and sizing process is laborious and time-consuming, but digital imaging and software advances have improved the process. Images captured with the SEM are stored digitally instead of transferred to film and then scanned into digital format. The counting and sizing process depends on the contrast of the particles from the background, which are most easily optimized on the SEM. This process was improved with practice. Even with image contrast optimized, the thresholding process to separate particulate from background can pick up incorrect results. Therefore, this process can not be automated because incorrect particles were manually erased from images. The Scion Image software then automatically sizes the particulate according to the parameters chosen. In this study, particles were approximated as spheres, so the only measurement used was area. This decision was based on the observations of the particulate, which did appear mostly spherical, except for amounts of molten material which were neglected.

1.3 Plasma Characterization

For any plasma application, characterizing the plasma is of the utmost importance for the understanding of the important phenomena. Particulate generation and textile modification are not exceptions. To potentially control the processes, the plasma must be characterized so that the relationship between the plasma and the process can be controlled. In particulate generation work, the main result to control is

the size of the particulate. The composition of the particulate is also important, which is more easily controlled by choosing the liner material.

Diagnostic methods for determining plasma parameters include voltage, current, and pressure measurements. The electrical parameters can lead to the determination of the plasma impedance and a simple circuit model of the plasma. Also, it is expected that the input energy plays a large role in the size of the particulate generated. The electrical measurements are vital for determining the energy input.

One of the most common and most important diagnostics tools, optical spectroscopy, can be used to determine the density and temperature of a plasma. These parameters are central to characterizing a plasma. For any plasma comprised of electrons, ions, and neutral species, it is important to understand the relative quantities of each. The domination of the plasma by a species impacts the characteristics.

In ET plasmas, the simplest spectroscopic technique is optical emission spectroscopy (OES). The SIRENS device, and the similar PIPE device have both been studied extensively with OES. A few of these studies include [11], [12], and [1]. While these past studies tended to focus on a time-integrated measurement taken at one location, measurements spanning radial and axial distributions were examined in [13]. Other pulsed plasma sources also studied the temporal and spatial evolution of a similar plasma [14].

Because of the extensive modelling in previous work, the aim of this work was not to develop a new model. Instead, estimates based on these models were used as quick plasma parameter checks. More extensive models can be used to compare measured with expected plasma parameters, but the quick parameter estimates are used to confirm the assumptions necessary for the analysis of diagnostic measurements. Neither the temperature or density are taken directly from spectroscopic measurements. Certain assumptions have to be made about the plasma before these parameters can be calculated. It is useful to verify these assumptions using simple calculations based on the electrical and mass measurements of the discharge.

Chapter 2

SIRENS Experiment and Theory

2.1 Device Layout

The SIRENS device consists of three main sections: the pulse-forming network (PFN), the plasma source section, and an expansion chamber. A diagram of the SIRENS experiment is shown in Figure 2.1 with detail of the source and barrel section seen in Figure 2.2. Both of these diagrams are taken from [8], because the initial setup was based directly on this work. The Fig. 2.1 was modified slightly to reflect changes made to the device, such as the addition of the access doors.

The PFN consists of a power supply, charging capacitor, high voltage trigger generator, spark gap switch, and the relays that isolate each part of the system and control the timing. The 300μF Maxwell Laboratories Energy Discharge Capacitor is charged to the desired voltage with a Sorensen high-voltage power supply and then discharged through a spark-gap switch through to the plasma-source electrode. A high voltage trigger generator provides 15kV output, creating the spark necessary to break down the air-gap in the switch and connect the capacitor to the source section. The inductance and capacitance of the system control the length of the pulse generated - in this case approximately 100μsec. The electrical characteristics of the system, namely current and voltage, are measured with a Pearson coil and high voltage probe.

The plasma source section consists of the tungsten alloy (DIMETECH or HD-17) cathode, Lexan insulator, sleeve, and expansion barrel. The Lexan insulator provides the insulation between the cathode and anode of the system. In this setup, the stainless steel expansion barrel used to support the pressure transducer also served as the anode. The insulation between cathode and anode forces an arc to form between cathode and anode in order to dissipate the electrical energy. The plasma is formed when the electrical energy input into the system leads the breakdown of the gas (air or otherwise) in the source section. The then conductive medium quickly transitions from a glow discharge to a thermal arc due to the high current present [8]. This process leads to the heating of the weakly ionized plasma. The

radiation from the heated plasma ablates the liner material, which then increases the plasma density. The pressure buildup leads to the plasma travelling out of the source and barrel section into the expansion chamber.

The liner sleeve material is traditionally Lexan or polycarbonate; however, almost any other type of material can be used so long as it is manufacturable into the correct dimensions. Conductive materials were of particular interest in this study, so aluminum and copper sleeves were used, in addition to Lexan and Teflon. When a single piece Lexan or Teflon sleeve was not used, the segmented sleeve, seen in Fig. 2.2, was used. The Maycor section was used to insulate the metal sleeve section from the cathode and because the ceramic resists ablation. The arc is forced through the capillary where it ablates mainly the material of interest.

The SIRENS expansion chamber is a 13" vacuum cross with a 20" extended section attached. Two eight-inch doors provide the main access to the chamber, so that the chamber can be fitted with a 180mm diameter glass expansion cell for the particulate collection. Multiple other diagnostic ports attached to the vacuum cross allow for the chamber pressure, the pressure transducer signal, and optical light emission to be measured.

To collect the particulate generated, the collection cell shown in Fig. 2.1 was used inside the vacuum chamber. This glass tube has a number of holes drilled through it that can be fit with threaded "buttons". The buttons can be fitted with any substrate material to collect particulate, and then easily removed from the system for analysis. Figure 2.3 shows the distribution of the buttons on the walls of the glass cell and on the endplate. This cell was designed for and used in [8], where the diagram of the button distribution also comes from. The buttons are distributed axially at distances 12.7, 31.75, 50.8, 69.9cm from the source section exit. The radial distribution places buttons at 3.0, 4.5, and 6.0cm from the center. The exact radial distribution seen in the diagram was not strictly adhered to, because previous work indicated that there was no significant trends in the radial direction.

Typical operation of SIRENS includes an under-damped current pulse with a peak current of 60 kA. In the past, electron densities were in the range of 10^{15} cm^{-3} with temperatures of approximately 1-3 eV. A summary of the operating characteristics is seen in Table 2.1, [8].

Table 2.1: SIRENS Operational Characteristics.

Discharge Voltage	1-8 kV
Peak Current	20-100 kA
Net Energy	1-80 kJ
Discharge Period	100-300 μsec
Radiated Power	2-120 GW/m^2
Peak Pressure	100-700 MPa
Plasma Density	$10^{24} - 10^{27} m^{-3}$
Average Temperature	1-3 eV
Average Velocity	4-8 km/s

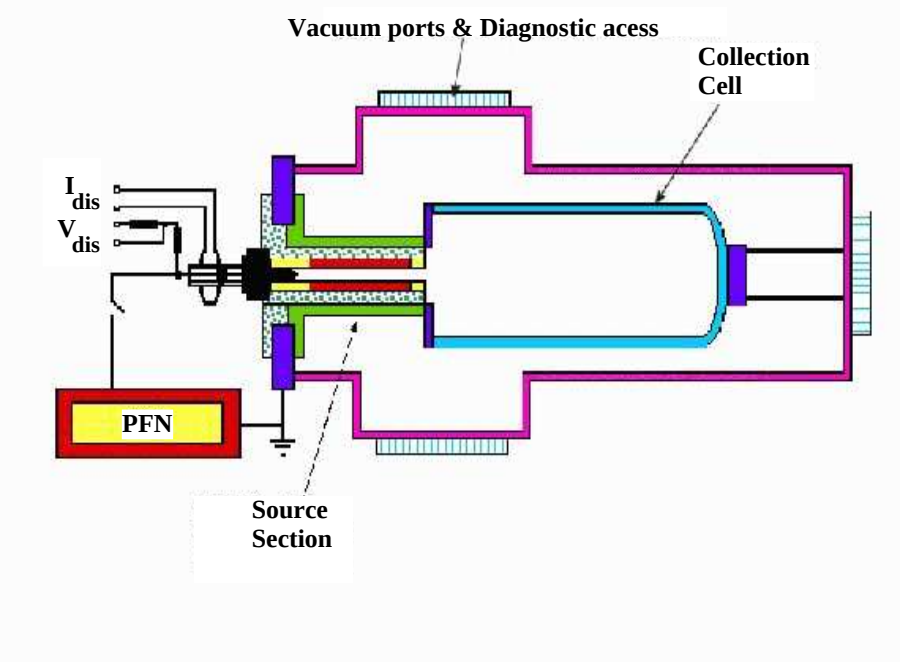

Figure 2.1: Schematic of the SIRENS Experimental Layout.

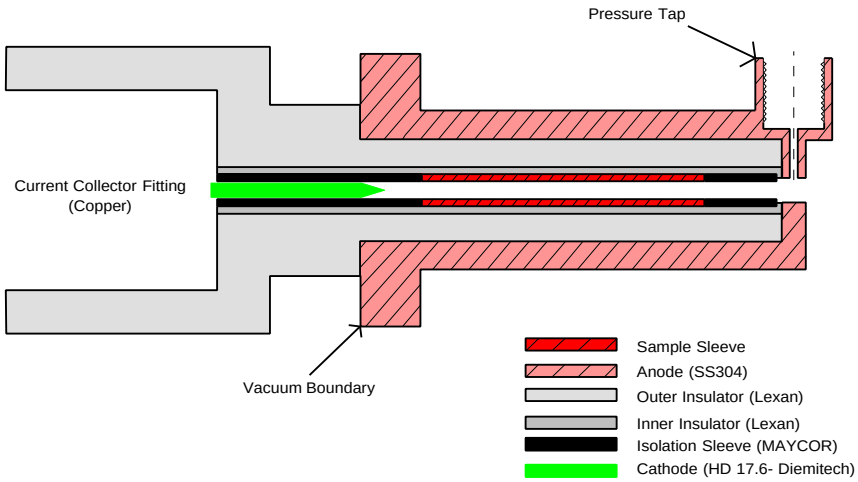

Figure 2.2: Detail of the SIRENS source and barrel section.

2.2 Diagnostics

The data acquisition system used on the SIRENS experiment consisted of a Tektronix TDS2024, a four channel digital oscilloscope. It provides 2 Giga samples per second data acquisition rate on each channel. The voltage was measured using a capacitively-coupled Tektronix high voltage probe. The current was measured using a Pearson coil. In addition to measuring the circuit behavior of the experiment, plasma

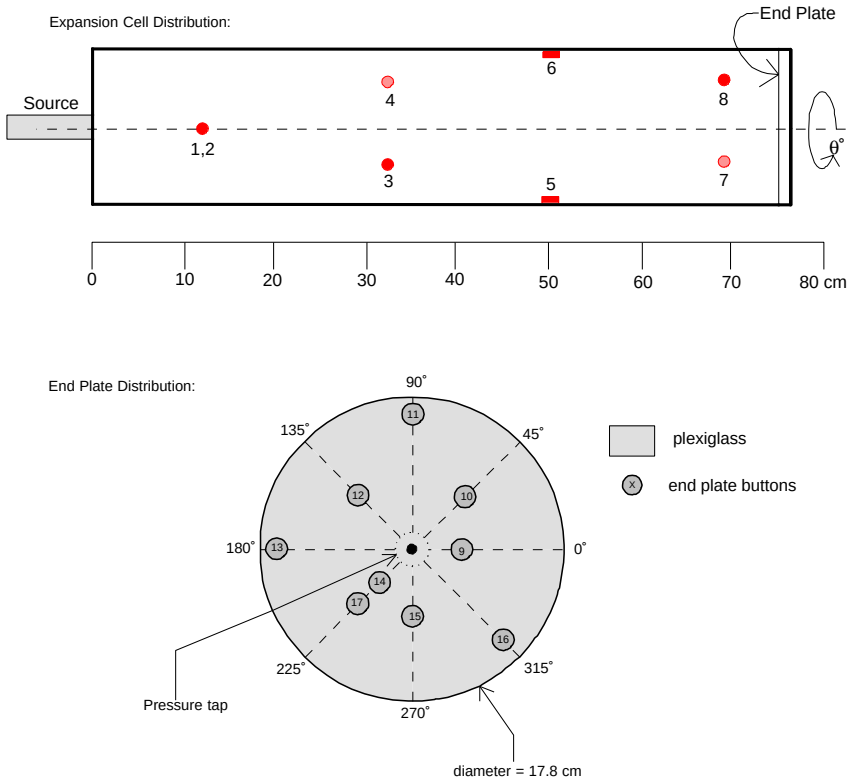

Figure 2.3: Schematic of the collection button distribution.

parameters such as electron density, n_e and electron temperature, T_e were measured using an Ocean Optics high resolution optical spectrometer (HR2000). The barrel exit pressure was measured with a Kistler piezoelectric pressure transducer. A single Langmuir probe was built and tested with the system, but an unidentified source of electronic interference made this diagnostic technique unusable.

2.2.1 High Voltage Probe

The high voltage probe (Tektronix P6015A) is a capacitively, compensated probe designed to optimize its frequency response to the input voltage up to a frequency of 75MHz by impedance matching. This is well within the frequency range of SIRENS, which is approximately 10 kHz. The probe has a resistance of 100 MΩ and a capacitance of 3.0pF with minimal inductance [15]. To measure the gun potential, V_{gun}, the probe was operated from a section of the cathode array to the common ground.

2.2.2 Pearson Coil

Pearson coils are current transformers that can be used to monitor fast current pulses. The Pearson coil used in these experiments was a wide band/pulse current monitor (Model 1423) with a 1000 amps/volt transform ratio. To record the current with the oscilloscope, the signal was also modulated with a 9:1

voltage divider. This model of current monitor is double shielded for the high voltage and high noise environment [16].

2.2.3 Pressure Transducer

A Kistler Model 617C piezoelectric pressure transducer was used to measure the pressure at the end of the source expansion barrel. The transducer was coupled to Kistler Type 501C charge amplifier. After some trial and error tests, the scale and sensitivity were set to 10,000 psi/V and 0.638pc/psi respectively. These settings resulting in the fewest overloads of the charge amplifier.

This type of piezoelectric transducer is meant for a high frequency pressure variation in environments such as gun barrels. The transducer works up to 75,000 psi and for approximately 2000 uses [17]. This pressure transducer was chosen because of its previous use in the work of [8]; however, a piezoresistive transducer might have been a better choice. Piezoelectric sensors can really only measure dynamic pressure, while piezoresistive sensors can measure static and dynamic [18].

The transducer's orientation with the face parallel to the plasma stream, indicated by the location of the pressure tap in Fig. 2.2, resulted in measurement of the static pressure. With this type of measurement, none of the dynamic pressure was measured. Additionally, because of the transducer's placement in the barrel section, the disturbance to the plasma flow was minimized and the perturbation of the local static flow can be considered equal to the total pressure from:

$$\Delta P_s = P_t - \Delta P_d, \tag{2.1}$$

where ΔP_s is the change in local static pressure, P_t is the total fluid pressure, and ΔP_d is the change in the local dynamic pressure) [13].

2.2.4 Langmuir Probe

A Langmuir probe is a conducting wire placed into the plasma to measure electron density and temperature and plasma potential. Since the wire, tungsten in these experiments, conducts current, the wire probe tip will accumulate charge if biased to a potential different from the plasma potential. Furthermore, a region known as the Debye sheath will envelope the probe tip. Quasi-neutrality will be violated in the local region around the probe tip because of the Debye sheath around the probe tip. A single Langmuir probe was built and tested in the SIRENS device; however, electrical interference prevented accurate measurement of the plasma signal. It was hoped that the probe would provide another measure of plasma temperature and density. Instead, optical spectroscopy was the only method of measurement used.

2.3 Optical Spectroscopy

In addition to electrical and pressure diagnostics, optical spectroscopy was used to obtain additional plasma parameters. Specifically, the plasma temperature and density were determined from optical emission spectroscopy. These measurements were taken for approximately the different axial locations at which particulate was gathered with the hope of correlating the plasma parameters to the particle size distributions calculated axially.

In previous research on SIRENS, both time-integrated and time-resolved measurements have been used to find the temperature and density of a variety of metallic and non-metallic plasmas [19]. A similar study was also performed on the electrothermal plasma device PIPE [13]. These, and other studies performed with the electrothermal devices, used the passive radiation technique of optical (or atomic) emission spectroscopy (OES). This method relies on radiation emitted by the plasma, or particles within the plasma. Other general methods include intrusive techniques and active radiation techniques. The Langmuir, or electrostatic, probe is an example of an intrusive technique. As previously described, this technique was attempted as a way to verify OES measurements, but was unsuitable in this study. Active radiation techniques rely on an external source of radiation as a probe of the plasma so that transmission, absorption, scattering, or reflection measurements can be made. The specialized equipment required made these techniques unsuitable as well [20].

The main drawbacks to OES analysis performed in the present work are the requirement for the plasma to be in local thermodynamic equilibrium (LTE) and the large uncertainty inherently contained in results from the method. The LTE assumption has been verified for the SIRENS device in multiple previous studies, and is assumed to hold true for the present study as well [6], [1]. The uncertainty in the results is a drawback for each of the methods described above, and can be minimized by choosing data sources appropriately.

In this work, only time-integrated measurements were obtained with an Ocean Optics High Resolution Spectrometer. This device has a grating of $600 lines/mm$ which is blazed at $500nm$ and has resolution of approximately $0.3nm$. The time-integration measures the light emitted over the full span of the discharge. Whether the values calculated from these measurements are an average or peak value has been raised, but not answered [19].

2.3.1 Temperature Measurement

The temperature of the plasma was measured using the relative line technique - by constructing a Boltzmann plot. Using the ratios of atomic, ionic, or molecular line intensities is one of the oldest techniques for determining the temperature of an LTE plasma [21]. In the present implementation of this technique, lines of varying intensities from atoms or ions of the same charge state are needed. The use of intensity ratios is based on the absolute intensity of a spectral line for the $m \rightarrow n$ transition being

proportional to the population of the excited state, the transition probability, and the energy of the emitted photons [22]:

$$I_{mn} = \frac{A_{mn}(E_m - E_n)g_n N}{Q} * e^{-E_m/kT_e}, \tag{2.2}$$

where A_{mn} is the transition probability in sec^{-1}, E_m and E_n are the upper and lower level state energies in Joules, g_m is the statistical weight of the upper state, N is the particle density of the species in m^{-3}, Q is the partition function, and T_e is the electron temperature in Kelvin. If the absolute line intensity, transition probability, statistical weight, and the density were known, then the temperature could be calculated directly. Since the density is not known via an independent measurement, taking the ratio of relative intensities provides a way to determine the temperature without knowing the density:

$$kT_e = \frac{E_{m1} - E_{m2}}{ln(I_2\lambda_2^3 g_1 f_1 / I_1 \lambda_1^3 g_2 f_2)}, \tag{2.3}$$

where f is the oscillator strength.

Another way to use relative intensities is to construct a Boltzmann plot from:

$$ln\left[\frac{\lambda I}{gA}\right] = C - E_i/kT, \tag{2.4}$$

where λ is the wavelength, I is the relative intensity, g the statistical weight of the upper level, A the transition probability, E_i the energy of the upper level, k is Boltzmann's constant, T the temperature of the plasma, and C an arbitrary constant [23]. So, the temperature of the plasma is determined from the slope of a line constructed from the Boltzmann factor, $ln\left[\frac{\lambda I}{gA}\right]$ versus the upper level energy, E_i. In addition, the linearity of the Boltzmann plot provides a proof that the plasma is in LTE.

The relative line method tends to suffer from large amounts of uncertainty due to the statistical weights. These values are experimentally determined, and can have as much as $\pm 50\%$ uncertainty. Another source of uncertainty is the line intensity. Determining the intensity of the lines used is usually a relatively simple procedure; a very complicated background, or continuum, shape could make the process more difficult. In addition, the number of emission lines used influences the accuracy of the fit. For instance, using only two points for a Boltzmann plot returns a perfect linear fit, but then there the temperature obtained is not believable.

2.3.2 Density Measurement

In addition to temperature, the density of a plasma is one of the most fundamental plasma characteristics, and is therefore very important for determining properties of the plasma. In the present work, measurement of the density and temperature can lead to a comparison with values obtained from simple models and past studies of similar plasmas.

Of the methods previously discussed, a passive method that disturbs the plasma as little as possible is

desired for accurate calculation of plasma conditions along the length of the chamber. The determination of density from OES measurements is more complicated than the determination of the temperature. Therefore, a more complete understanding of the background theory is necessary for understanding why OES was an appropriate diagnostic choice and why the particular analysis method was chosen for the determination of the plasma density in the SIRENS device.

In general, the density of a plasma can be related to the widths of measured lines. The profile of a line is influenced by several broadening mechanisms including Doppler, Stark (or pressure), natural, and instrument broadening. For a plasma in LTE, Stark broadening is usually the dominant type. Other types of broadening, such as Doppler broadening, can be neglected [22]. This is true with the caveat that Doppler broadening is important, and usually dominant in multiply ionized species in dense plasmas [22]. However, the plasma generated by the SIRENS experiment consists almost exclusively of neutral and singly ionized species. The natural broadening of a line is far below the resolution of the spectrometer used in this work. The instrument broadening is the one other mechanism which can not be neglected. However, it is easily measured and accounted for in the analysis.

The use of Stark broadening to determine the plasma electron density is one of the most widely used diagnostic techniques in both laboratory and astrophysical plasmas. The broad range of applicability has been studied since the 60's or 70's, leading to extensive development of the theory and comparison with experimental results in studies such as: [22], [24], [25], [26], [27], [28]. A short review of this theory is important for understanding the model used to analyze the experimental data.

The basic terminology in line broadening refers to emitters and perturbers - the emitter being the atom or ion emitting the radiation caused by the perturbing particle. Based on the Stark effect, the density of a plasma is related to a line width via the density of charged particles surrounding an emitter [28]. The most commonly and therefore best studied lines for this purpose are the hydrogen lines. The hydrogen lines are so important in Stark broadening because of the linear Stark effect for hydrogen atoms and ions - the density of a plasma and the FWHM of the hydrogen line are linearly related [27]. The Hβ line is considered the best line to use, because: (1) the Stark broadening is very strong, (2) there is almost no self-absorption affecting the shape of the lines, and (3) the broadening of the line is barely affected by the movement of ions, or ion dynamics. Unfortunately, the line, at 486nm, occurs in a region containing many other lines and can be difficult to isolate and fit. In situations where the Hβ line is difficult to resolve or too weak, the Hα line at 656.3nm can be used instead. While the Hα line can be stronger and less convolved with other lines, the drawbacks include: (1) the Stark broadening is less strong than for Hβ at the same density (2) self-absorption can be important, and (3) broadening due to ion dynamics can be strong [28].

The last drawback listed for the Hα line has been the focus for much of the most recent research into Stark broadening. The research into ion dynamics deals with the theory of hydrogen line broadening. Luque et al, [28], provide a very good history of the different approximations used to model this broad-

ening. In general, the different approximations are based on the average time of a collision being larger or smaller than the average time between collisions, or the speed of the perturbing particles [27].

The first approximation, called the quasistatic approximation, assumes that the average collision time is the larger value; so the approximation is valid for ionic perturbers. This approximation results in a line profile which is a Holtsmark function - valid for the wings of the line profile. This approximation was the first studied, when computational methods were not available to account for ion dynamics. The second approximation, known as the impact approximation, is in general for fast, light, and highly mobile perturbers such as electrons. The line profile resulting from this approximately instantaneous collision is Lorentzian, and is therefore valid at the center of the line profile [28].

Two main implementations of these approximations result in formulae and tables of data necessary for the calculation of density from measured full-width half max (FWHM) values. The Kepple-Griem theory, [29], tries to convolve both approximations so that the line profile follows:

$$S_{n'n}(\alpha) \approx \frac{C_{n'n}}{|\alpha|^{5/2}} G_{n'n}(\alpha), \tag{2.5}$$

where α is the reduced wavelength ($\Delta\lambda/E_0$); n' and n are the upper and lower transition levels; $G_{n'n}(\alpha)$ is the term group correcting the profile depending on α, $n'n$, the electron temperature, and density; and $C_{n'n}$ is a constant that defines the Holtsmark profile. Values for $G_{n'n}$, $C_{n'n}$, $S_{n'n}(\alpha)$, and $\alpha(n_e, T_e)$ are tabulated in [25]. Then, the FWHM of a Stark line is found from:

$$w_s = 2.50(10)^{-10} \alpha_{n'n}(n_e, T_e) n_e^{3/2} \quad (nm), \tag{2.6}$$

for electron density values in cm^{-3} [28].

Comparisons of the Kepple-Griem theoretical line profiles with experimentally observed profiles showed that the Hα lines were broader than the tables predicted, especially at low densities [27]. These differences were attributed to the movements of ions, knowing that ion dynamics were left out of the theory. Two basic models were developed to account for ion dynamics - the model microfield method (MMM) and the reduced mass ion model; again, [28] provides a good overview of each model. Neither of these models are based on new plasma models, they just include the effects which were previously left out of the approximations. The reduced mass, or μ, ion model is the most recent computational model developed. It is based on emitter-ion pairs characterized by the reduced mass, μ, for the pair. Compared to the MMM, the μ-ion method overestimates the effects of ion dynamics. This is not of great importance when analyzing a dense plasma such as an electrothermal plasma, because the ion dynamic effect is only very important at low densities, below $n_e = 10^{14}$ cm^{-3} [28].

Even though the ion dynamics effect is not expected to be large at the densities of the SIRENS plasma, the μ-ion model used in [27] was chosen to calculate the density. This procedure was used in similar situations, such as [14]. Based on [30], $\mu = 1$ was used, corresponding to a hydrogen emitter in

a mixture of heavier ion perturbers.

The data in Table 2.2 was plotted to determine fits to the data in [27], as seen in Figure 2.4. As expected for the Stark effect on a hydrogen line, the density is linear with the width of the Hα line, and there is very little dependence on temperature. Therefore, using the temperatures calculated via the relative method, the plasma density could be determined from the FWHM of the Hα line.

Table 2.2: Temperature comparison FWHM's of Balmer-α (in nm) for μ=1 from [27].

log(N_e) (m^{-3})	at 5000K	at 10000K
20.00	0.0144	0.0143
20.33	0.0234	0.0244
20.67	0.0370	0.0401
21.00	0.0582	0.0634
21.33	0.0906	0.100
21.67	0.141	0.158
22.00	0.220	0.246
22.33	0.350	0.386
22.67	0.570	0.611
23.00	0.958	0.992
23.33	1.61	1.66
23.67	2.77	2.82
24.00	-	4.83
24.33	-	8.27

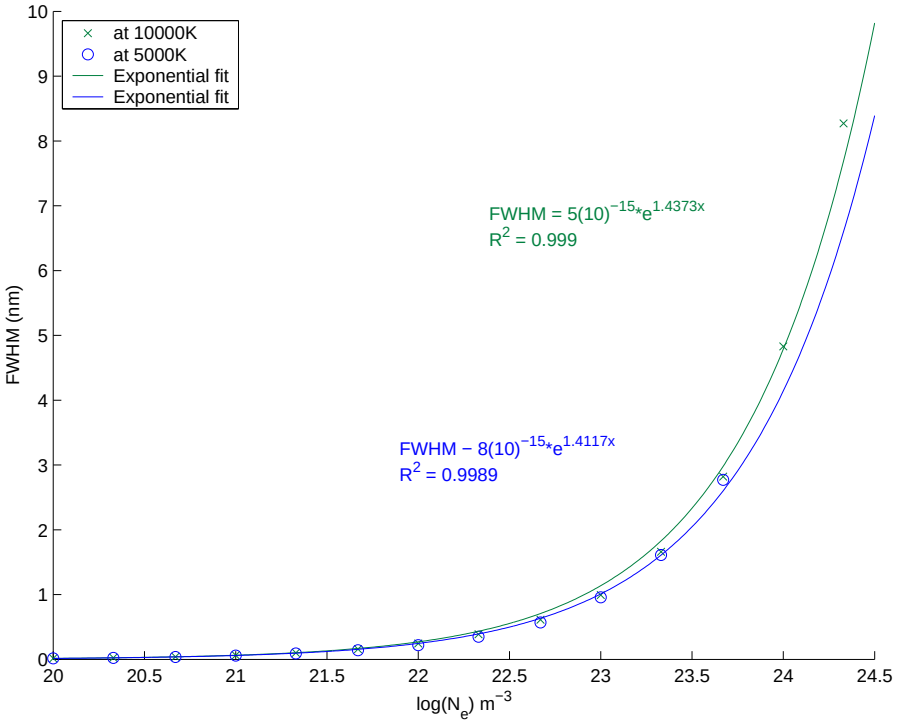

Figure 2.4: Plot of temperature comparison of Hα FWHM for T=5000 and 10,000K with μ=1

In addition to hydrogen lines, the plasma density can be obtained for the width of other neutral atom lines having approximately Lorenztian shapes. In both the hydrogen and heavier atom lines, the line width (FWHM) is determined using the PeakFit software and the instrument broadening so that [31]:

$$\Delta\lambda_{true} = \Delta\lambda_{observed} - \Delta\lambda_{instrument}. \tag{2.7}$$

Then, to determine the electron density within 20-30%:

$$\Delta\lambda = 2W\left(\frac{N_e}{10^{16}}\right) + 3.5A\left(\frac{N_e}{10^{16}}\right)^{1/4}, \tag{2.8}$$

where W is the electron impact width parameter and A is the ion-broadening parameter which can be neglected for non-hydrogenic plasmas.

For the neutral copper lines visible in many of the spectra obtained, the W and A parameters could not be found in literature. However, the stark widths and shifts have been compiled and can be found for many neutral and singly ionized atoms.

The values of the Stark widths and shifts are found at certain densities - usually 10^{16} or 10^{17} cm^{-3}. The values are also found at different temperatures, but there is only a very weak dependence on temperature. Therefore to calculate the plasma density, the nominal density is multiplied by the ratio of measured width to the Stark width:

$$n_e = \frac{\Delta\lambda_{true}}{w_m} * 10^{23} m^{-3}. \tag{2.9}$$

Based on previous work with similar electrothermal plasma sources, it was expected that the temperature would remain somewhat constant over the length of the measurements [13]. In addition, the pressure for this type of flow is expected to drop as a function of $1/r$ where r is the distance from the plasma source. Therefore, because the plasma pressure is defined as $P = nkT$, the plasma density should also be a function of $1/r$.

Chapter 3

Particulate Generation and Characterization

3.1 Particulate Generation

A variety of materials were used as ablators from which particulate was generated, including: aluminum, copper, Lexan (polycarbonate), and Teflon. The first test was performed with an aluminum fuse, which is a common method in this type of device. However, all subsequent tests were performed with the liners described in the previous chapter. The Lexan and Teflon sleeves were a single piece, but the metal sleeves were segmented, following the diagrams of [8]. The Maycor segment in each sleeve was used to insulate the cathode from the metal segment. In addition, Maycor resists ablation, so the plasma consists mainly of the material of interest.

For all shots, all pieces of the liner were massed pre- and post-shot on a microbalance with a tolerance of ± 0.05mg. For most shots, the Maycor insulator shattered during the shot due to the elevated temperature, so no post-shot mass was obtained. Many times the outer Lexan sleeve which held the rest of the sleeve assembly was also destroyed to retrieve the other liner pieces. No ablation was expected from the outer sleeve, so the destruction was accepted when necessary to retrieve the inner sleeves.

For shots with buttons, the buttons were cleaned in an ultrasonic cleaner before being massed pre-shot. As with each sleeve piece, each button was massed at least three times and the average was taken as the recorded mass. Once cleaned, the buttons were kept in covered petri dishes until just before the shot when they were attached to the button holders, placed in the expansion chamber, and finally placed into the device for the shot. The buttons were also handled with tweezers to maintain cleanliness. The buttons were attached to the button holders with rubber cement following the procedure described in [8]. A set of test buttons was used to test the attaching procedure, and no discernible mass gain was measured; the largest mass difference recorded was 0.04% for the control buttons. After the shot and

the removal of the expansion chamber from the device, the buttons were removed from the holders and placed in the petri dishes before being massed again. Any glue remaining on the buttons after removal from the button holders was removed with acetone.

The fabrics and PET film used to cover the buttons were washed with alcohol or acetone and allowed to dry before being glued onto the backing and massed. While the mass gains for the uncovered buttons were generally consistent, there were many incidents where fabric covered buttons appeared to have lost mass after exposure to plasma. The subsequent SEM images showed particulate accumulation; however, the measured mass loss could be due to glue evaporation. The rubber cement used to attach the buttons to the holders was convenient because of the ability to easily remove the buttons and clean off any remaining glue, but a different glue for the fabrics might be better. Also after exposure, several fabric samples went through a washing test to explore the fastness of the particles to the surface. The AATCC Test Method 61-1993 was utilized. Specifically, test number 2A was performed in a Launder-Ometer [32].

While several types of fabrics were exposed to the plasma, only one pattern transfer test was attempted. A simple pattern was cut from a sheet of Mylar and attached to a piece of fabric. When exposed to the plasma, both the pattern and the fabric were partially destroyed. This was most likely due to the material of the pattern and the placement of the pattern on the fabric. The areas of the fabric exposed to the plasma and not destroyed did show evidence of particulate deposition. However, as with other metal deposition tests on fabric, no continuity was measured with a multimeter. The metal particulate was not sufficient to provide a measurable conductivity to the fabric.

3.2 Particulate Characterization

After generating particulate and re-massing the collection buttons, the next step was the characterization of the particulate. Characterization was performed with SEM and Energy Dispersive X-ray imaging (EDX), particle counting, and generating particle size distributions. Each of these steps will be discussed.

3.2.1 SEM Images

After re-massing the buttons, the next particulate characterization step was to obtain SEM images of many of the buttons. All of the SEM images were obtained with a Hitachi S3200 environmental SEM in the Analytical Instrumentation Facility at NCSU. The flexibility of the environmental, or variable pressure, SEM allowed for the imaging of the fabric covered buttons without coating the surfaces with a conductor. This was convenient and does not destroy the samples - allowing for future examination. In addition, the SEM could easily switch between environmental and vacuum operation so that many samples, including metal and fabric-covered buttons, could be loaded at once and save time.

Initial imaging attempts resulted in images where the particles were difficult or impossible to count

and size – especially for particles on stainless steel buttons where the grain boundaries interfered greatly. The contrast and brightness on the SEM were eventually optimized to produce images which could quickly be counted and sized. Also, the initial micrographs's lacked the standardization of the magnifications used in later images to accurately capture the full range of particle sizes.

When time allowed, buttons from each axial distance were imaged so that size distributions with distance from the source could be calculated. Also, important for the accurate representation of the particulate size distributions was to capture the full size range of particles. As discussed in [8], increasing magnification records smaller particles, but the density of particles per image also greatly decreases. Imaging at 500x, 1200x, and 3000x was confirmed to capture the full range of particles while maintaining a significant amount of particulate per image. Optimally, four images from different locations on a button at each magnification should be obtained for each button. However, this proved too time-consuming to perform for every shot. Nonetheless, particulate was counted for every button where background and particulate were separable.

3.2.2 Particle Sizing

Scion Image, essentially the NIH Image software for the Windows operating system, is standard software used to count particles. For particulate counting with the software, each image is scaled and the contrast and brightness adjusted so that only the particulate is highlighted when a threshold is applied. The thresholding method used in this work converted the gray-scale image into black and white so that the particulate could be counted and sized. The particulate can be characterized by a number of features including area, ellipse major and minor radii, and perimeter. For the present study, only the area measurement was used, and then each particle was approximated as spherical so the diameter was taken from the simple formula $A = \pi d^2/4$.

3.2.3 Particle Size Distributions

Once the particles were counted and sized for a button, then particle size distributions could be generated. The software programs Excel and KaleidaGraph were used to generate these distributions. Excel was used to record and summarize the data, while KaleidaGraph was used to generate the distributions. The KaleidaGraph probability plot displayed the percentage of particles that were smaller than a certain size; a log-normal probability distribution to the data was assumed. A linear fit was then applied to the data in the plot to return the particle size distribution fitting parameters. The curve fit was of the form:

$$d = a * exp(b * norm(x)), \tag{3.1}$$

where a is the median particle size, b is the standard deviation of the normally distributed data, and norm(x) determines the normal distribution of a number between 0 and 100%. As in [8], the particle

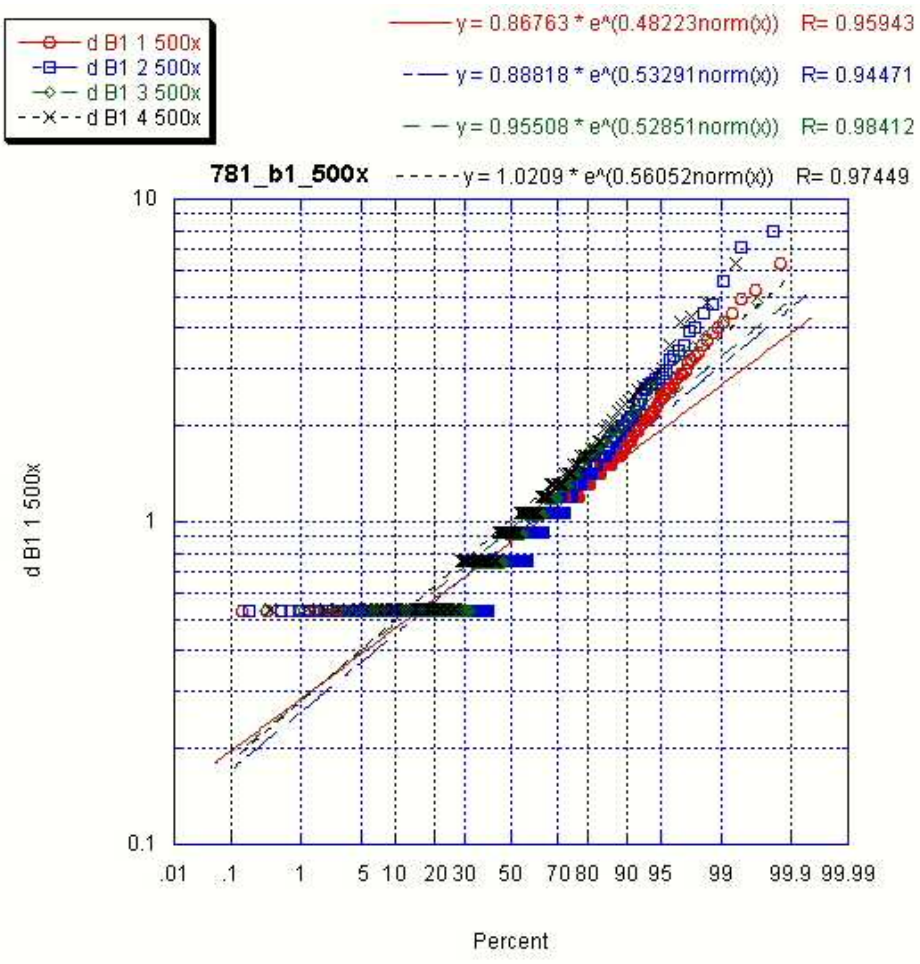

Figure 3.1: Aluminum shot S781 particle distribution for button 1 at 500x magnification

diameters reported from these fits are $d_{15.9\%}$ or count median diameter (CMD), $d_{50\%}$ or median particle size, and $d_{84.1\%}$. Figures 3.1 – 3.3 show examples of the distributions developed. The full graphical distributions are not presented for every buttons to conserve space. The distributions represent the percentage of particles whose diameter is less than a certain value.

Besides the diameters of interest, the geometric standard deviation (GSD) and the linear correlation coefficient, R^2, values from the fits are also reported for each shot. For the log-normal distribution, the GSD is $d_{84.1\%}$ divided by $d_{50\%}$ [8]. While the particles were counted from images at different magnifications, these distributions were developed by combining all of the data so that the full range of particle sizes would be encompassed. Also, when multiple images on one button were obtained at the same magnification, all of the measured diameters were combined for a more accurate distribution.

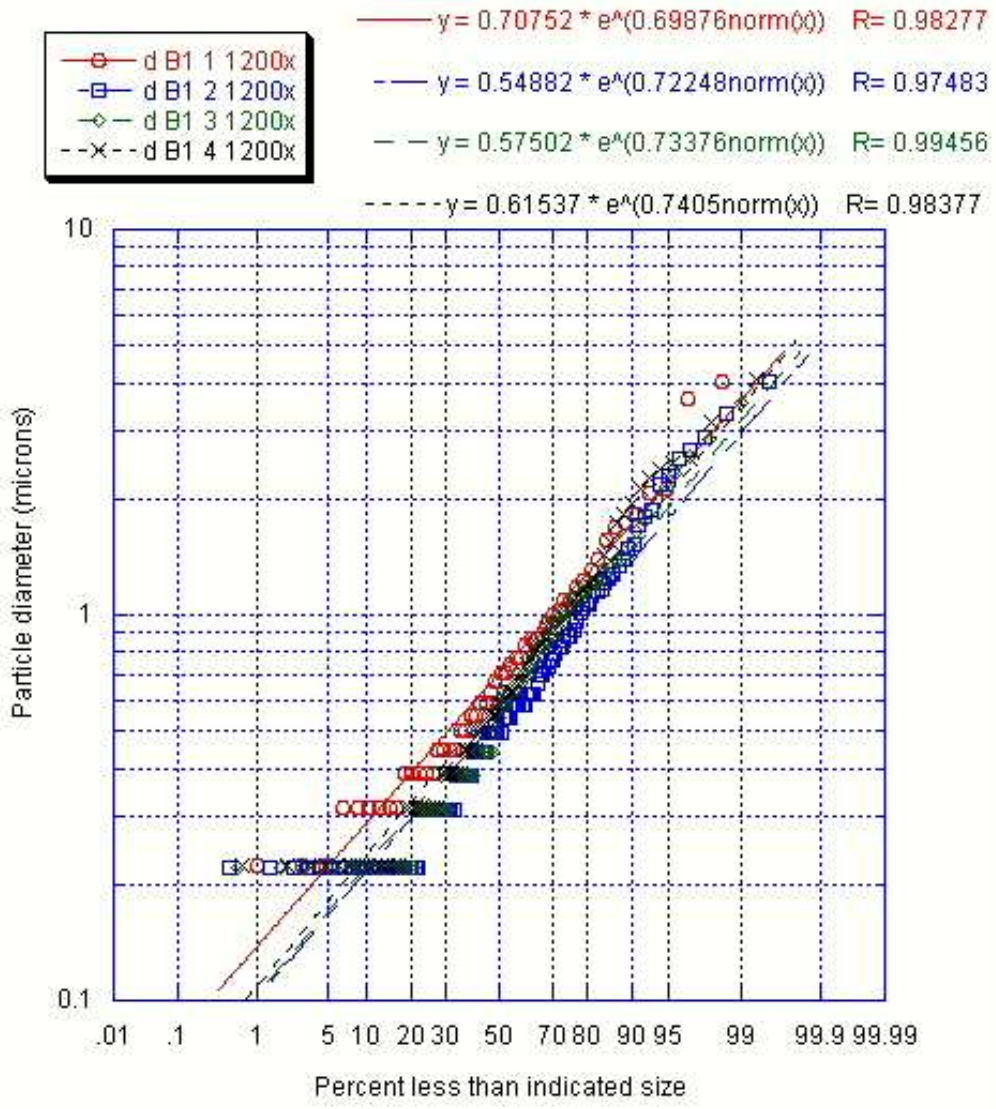

Figure 3.2: Aluminum shot S781 particle distribution for button 1 at 1200x magnification

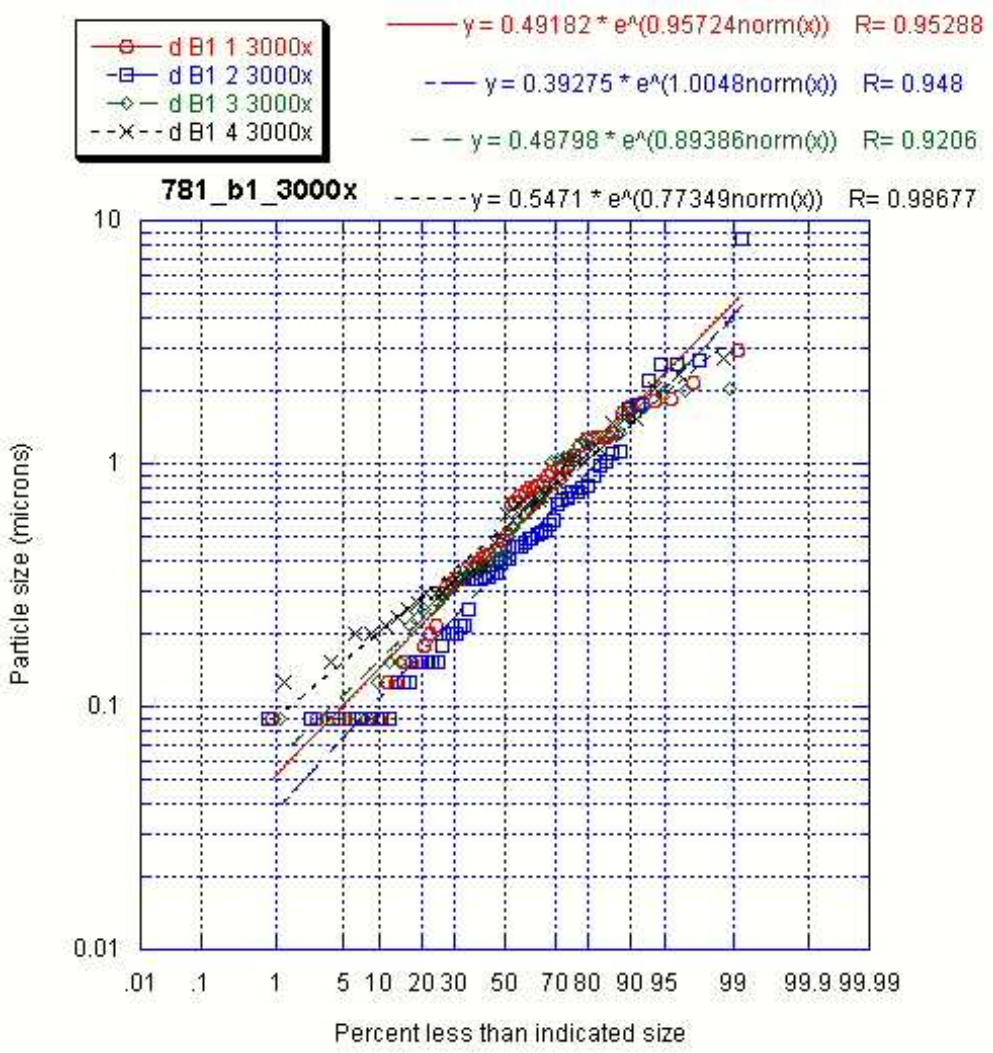

Figure 3.3: Aluminum shot S781 particle distribution for button 1 at 3000x magnification

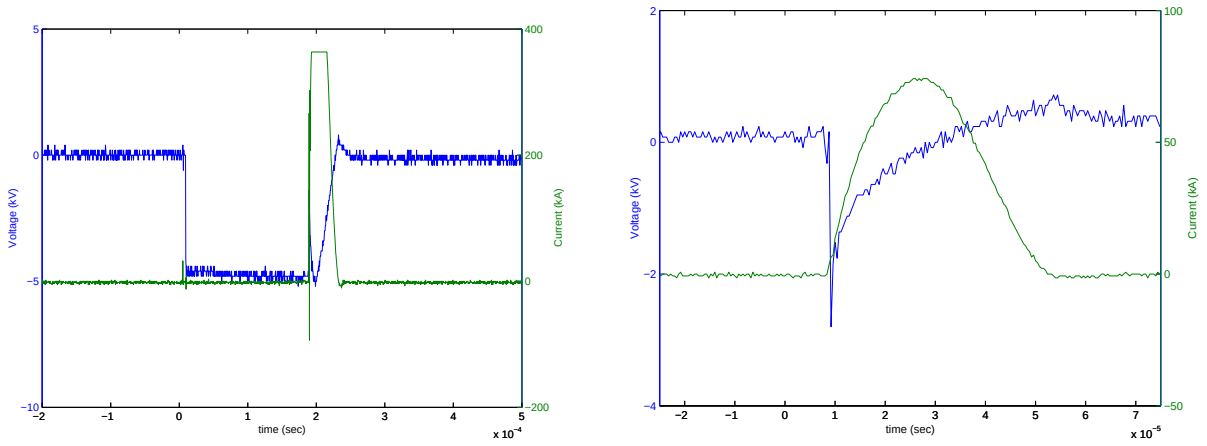

(a) S782 (b) S799

Figure 3.4: Plots of aluminum shots sample current and voltage traces.

3.3 Aluminum

3.3.1 Overview

Shot S780 used an aluminum fuse instead of the segmented liner of shots S781, S782, and S785. Typical current and voltage traces are seen in Fig. 3.3.1. The traces for shot S782 were clipped because the appropriate oscilloscope settings had yet to be worked out. Shot S799 was an aluminum shot taken to acquire spectra, but the electrical characteristics are equivalent to the aluminum shots taken for particulate generation. The net input energies of the shots were 2.636 kJ, 5.725 kJ, 3.690 kJ, and 5.725 kJ - calculated from the voltage difference on the charging capacitor pre- and post-shot. Except for shots S780 and S782, all of the shots taken for this work were at approximately the same energy, 5.7 ± 0.14kJ. The shot energies and other relevant data are summarized in table 3.1. Shots S780-S782 included 17 buttons each, the first two employing only copper buttons, but shot S782 included the first fabric test with 6 nonwoven fabric covered buttons. Shot S785 was not a test for particulate accumulation, but included one large piece of cotton fabric along the entire length of the interior. The test, performed for Brian Bures, attempted to determine if the particulate would help form a fluorocarbon surface. No benefit was determined, so the test was not repeated. From the button mass difference measurements in Table 3.1, the fuse in shot S780 produced less mass accumulation on the buttons. This is expected from the initial mass of the fuse and the geometry. Aluminum cannot be ablated from an exploding fuse.

3.3.2 Particulate Observation

In general, the aluminum shots resulted in significant particulate accumulation, which can be seen on the copper buttons for shot S781. Representative images of the particulate captures are seen in Figs. 3.5

Table 3.1: Aluminum button mass difference summary.

	Al Shot S780	Al Shot S781	Al Shot S782
Energy (kJ)	2.636	5.725	3.690
Sample Δm (mg)	fuse destroyed	530.72	76.0
Cathode Δm (mg)	77.2	53.5	broke into pieces
	Δm (mg)	Δm (mg)	Δm (mg)
Button 1	0.04667	0.15667	7.74333
Button 2	0.05667	0.15667	0.05000
Button 3	-0.01333	0.25667	7.69583
Button 4	0.02667	0.27500	0.12750
Button 5	0.02667	0.33667	0.05750
Button 6	0.02000	0.27000	0.04333
Button 7	0.03833	0.30333	6.82000
Button 8	0.04500	0.18000	0.46583
Button 9	0.37000	0.77333	6.81667
Button 10	0.14667	0.75333	6.76333
Button 11	0.17333	1.04417	-3.51750
Button 12	0.14667	0.48250	-6.59250
Button 13	0.23667	1.00250	2.66333
Button 14	0.49667	0.62167	9.98833
Button 15	0.12333	0.52667	2.77500
Button 16	0.32667	0.86667	6.16667
Button 17	0.17667	0.33917	-8.45000
Button 18			7.24917

and 3.6. The first image shows a common feature of aluminum shots where molten material impacted the button surface and the material rolled along the surface as it cooled. Then what was left on the surface was a streak of aluminum. On the fabric in Fig. 3.6, the material could not roll along the surface and so only distinct particles were left. The streaks and other features left from molten material are not surprising considering aluminum's low melting temperature.

Tables 3.2 and 3.3 show the results of the cumulative particle size distributions. Only the approximately spherical aluminum particulate was counted and sized; images were carefully recorded to avoid as many irregular features as possible. The first table shows the detail of each button and each magnification used. Later tables combine this data and present only the overall distribution for a button. From this table, it is useful to note the different average size particulate observed for each magnification. The less magnification, the larger the particles observed. This table is a quick confirmation for why a range of magnifications must be used to capture the full range of particulate sizes. Also apparent in Table 3.2 are several size trends. First, it appears that the smallest particulate at each magnification remains approximately constant with distance from the source. On the other hand, there is a slight increasing trend for for the average and larger particulate with increasing distance from the source. The data in Table 3.3 is not as complete, and the same types of inferences cannot be drawn. Although, when the magnifications are somewhat similar between the two shots, the particle sizes are comparable.

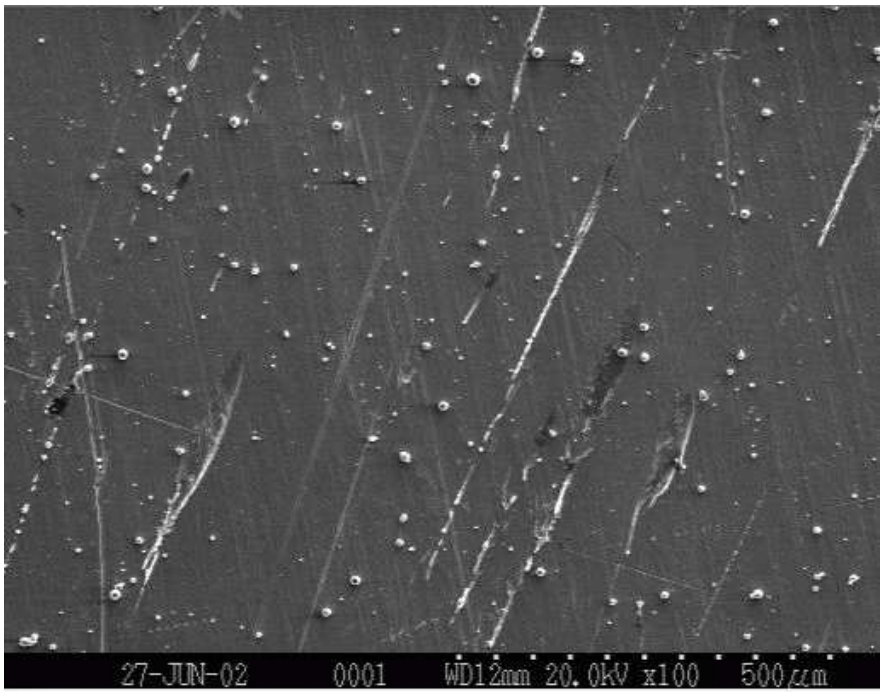

Figure 3.5: SEM image of aluminum particulate from shot S781 on copper substrate, with streaks.

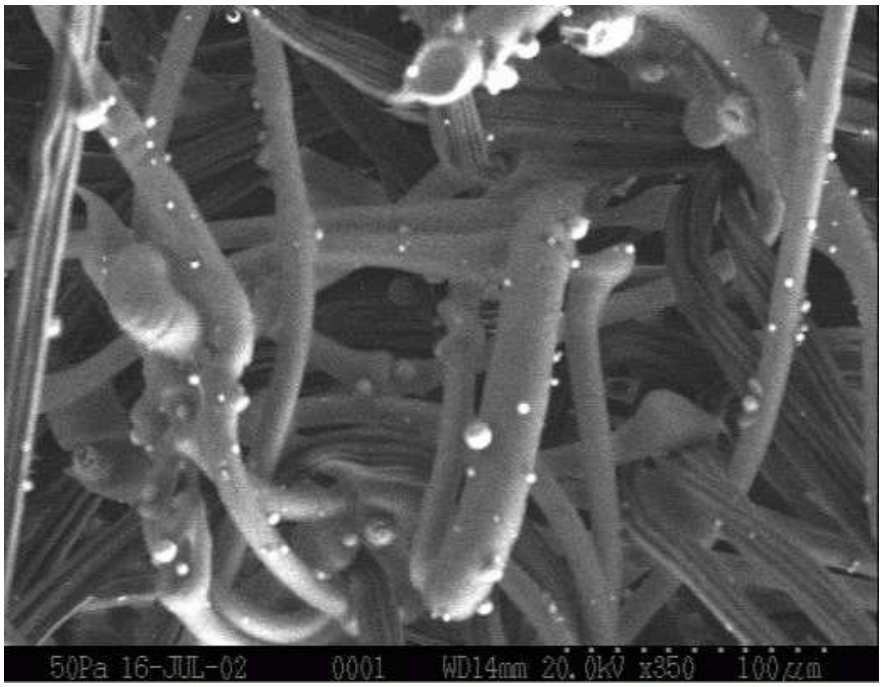

Figure 3.6: SEM image of aluminum particulate from shot S782 on nonwoven fabric.

Table 3.2: Aluminum particulate analysis summary from shot S781.

Button	Axial Distance (cm)	Mag., # of images	$d_{15.9\%}$ μm	$d_{50\%}$ μm	$d_{84.1\%}$ μm	GSD	R^2
1	12.7	500x, 4	0.52	0.86	1.43	1.663	0.905
1	12.7	1200x, 4	0.27	0.56	1.17	2.090	0.985
1	12.7	3000x, 4	0.18	0.44	1.08	2.455	0.916
4	31.75	500x, 2	0.60	1.13	2.12	1.876	0.958
4	31.75	1200x, 2	0.36	0.82	1.86	2.268	0.985
4	31.75	3000x, 2	0.14	0.45	1.49	3.311	0.959
5	50.8	500x, 4	0.53	0.98	1.80	1.837	0.895
5	50.8	1200x, 4	0.30	0.68	1.55	2.279	0.965
5	50.8	3000x, 4	0.20	0.57	1.64	2.877	0.973
8	69.9	500x, 2	0.57	1.31	3.02	2.305	0.966
8	69.9	1200x, 2	0.36	1.08	3.22	2.981	0.858

Table 3.3: Aluminum particulate analysis summary from shot S782.

Button	Axial Distance (cm)	Mag., # of images	$d_{15.9\%}$ μm	$d_{50\%}$ μm	$d_{84.1\%}$ μm	GSD	R^2
2	12.7	300–4000x, 5	0.33	0.96	2.75	2.865	0.972
3	31.75	900,2000x, 2	0.25	0.75	2.22	2.959	0.923
4	31.75	120,350x, 2	1.53	3.09	6.26	2.026	0.954
8	69.9	180,200x, 2	1.52	2.82	5.22	1.853	0.972
17	endplate	350–3000x, 5	0.49	1.17	2.80	2.400	0.996

3.4 Copper

3.4.1 Overview

Shots S788 and S790 were the only shots with copper liners which were not for the purpose of acquiring spectra. Shot S788 included stainless steel and woven fabric covered buttons. Shot S790 was a shot to test the Langmuir probe circuit. Although the probe did not work, electrical data was still obtained. The current and voltage traces for both shots are seen in Fig. 3.4.1. The net input energy for both of these shots was 5.8kJ. The relevant mass measurements are presented in Table 3.4.

3.4.2 Particulate Observation

Compared to aluminum sleeves, the copper sleeves ablated less mass. This could be due to the higher melting point of copper. Another indication of no melting was that the copper did not form the same streaks as aluminum. So, there was much less, if any, molten material in the plasma stream. Figures 3.8–3.10 represent typical SEM images of copper particulate on the different substrates used. Table 3.5 presents the cumulative particle size distributions for the images on which particulate was countable. On average, the particle sizes are less than those measured for aluminum particulate. However, many fewer images from only one shot contributed to the size distributions for copper. Without more particulate to count it is impossible to determine if smaller particulate is a feature of copper shots or just insufficient

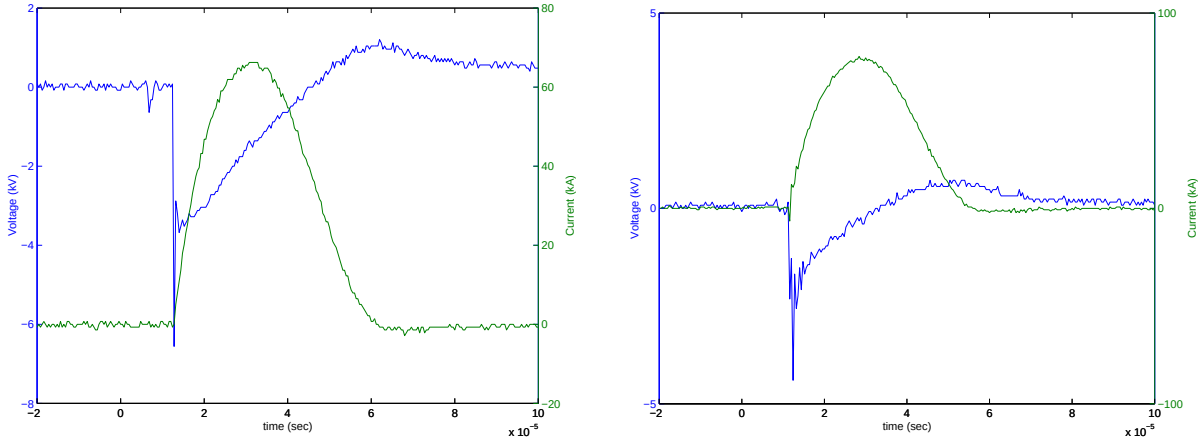

(a) S788 (b) S790

Figure 3.7: Plots of copper shots sample current and voltage traces.

Table 3.4: Copper button mass difference summary.

	Cu Shot S788	Cu Shot S790
Energy (kJ)	5.822	5.838
Sample Δm (mg)	–	−414.2
Cathode Δm (mg)	–	−9275.2
	Δm (mg)	Δm (mg)
Button 1	0.20833	—
Button 2	−0.12667 (fabric)	—
Button 3	0.14667	—
Button 4	0.08500 (fabric)	—
Button 5	0.04833	—
Button 6	0.69000 (fabric)	—
Button 7	0.42667	—
Button 8	0.33750	—
Button 9	0.46667	—
Button 10	0.41083	—
Button 11	0.27917	—
Button 12	0.2600	—

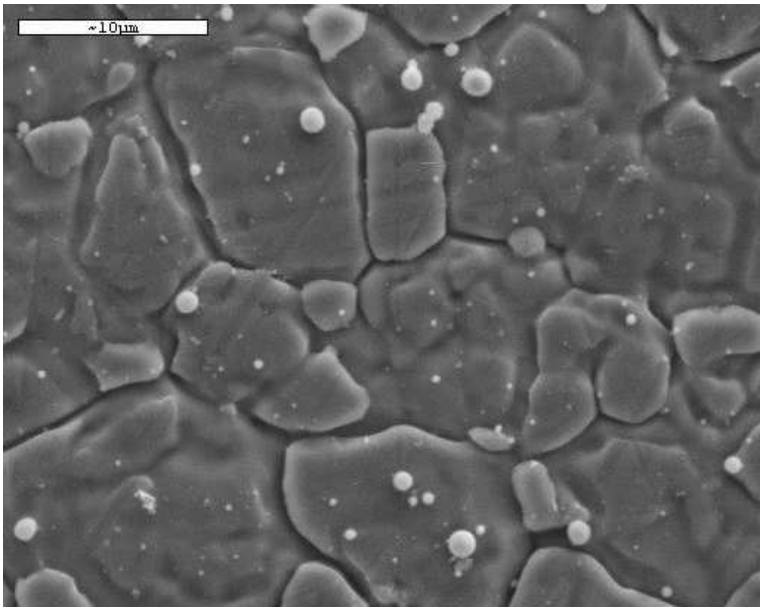

Figure 3.8: SEM image of copper particulate on stainless steel button from shot S788.

Table 3.5: Copper particulate analysis summary from shot S788.

Button	Axial distance (cm)	Scale (pixel/μm)	$d_{15.9\%}$ μm	$d_{50\%}$ μm	$d_{84.1\%}$ μm	GSD	R^2
2	12.7	7.55, 6.4	0.19	0.36	0.70	1.92	0.963
3	31.75	12.7	0.11	0.26	0.60	2.31	0.984
5	31.75	12.7	0.086	0.18	0.37	2.06	0.988
6	50.8	1.7, 6.3	0.59	1.00	1.69	1.69	0.987

data.

3.5 Mixed Materials: Aluminum/Copper

3.5.1 Overview

The mixed materials shots were performed with a half aluminum, half copper sleeve made by milling away, lengthwise, half of each type of full liner. Particulate was collected from two shots – S789 and S791. Both stainless steel and woven fabric covered buttons were used in shot S789 to collect particulate. Stainless steel buttons were used in shot S791, in addition to the endplate pattern transfer test previously discussed. The button mass difference values are indicated in Table 3.6. The net input energy to both of these shots was approximately 5.8kJ, as in the copper shots. When a shot was performed with a metal liner material, the charging capacitor discharged very completely, so that by choosing the initial potential, the net input energy could be very well controlled. This is convenient for shot comparison purposes, and allowed for almost all of the shots taken to be at the same energy, within 2.5%. Current

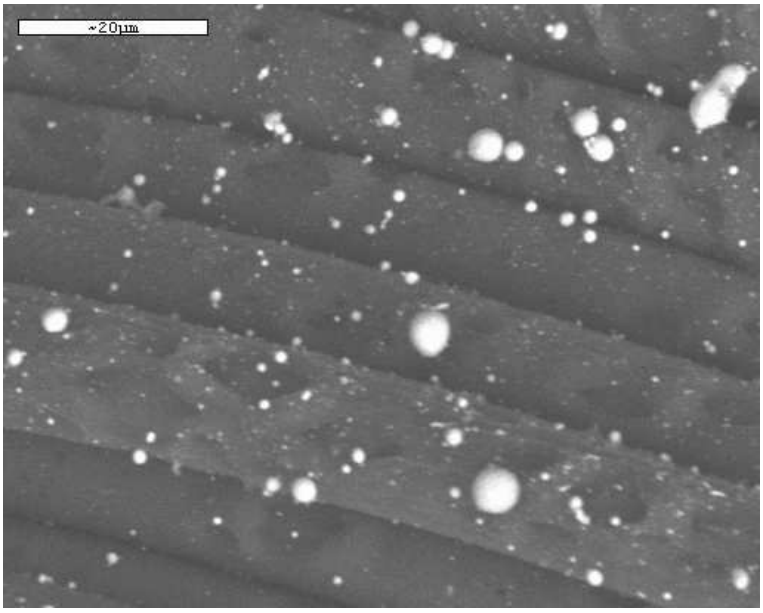

Figure 3.9: SEM image copper particulate on woven fabric from shot S788.

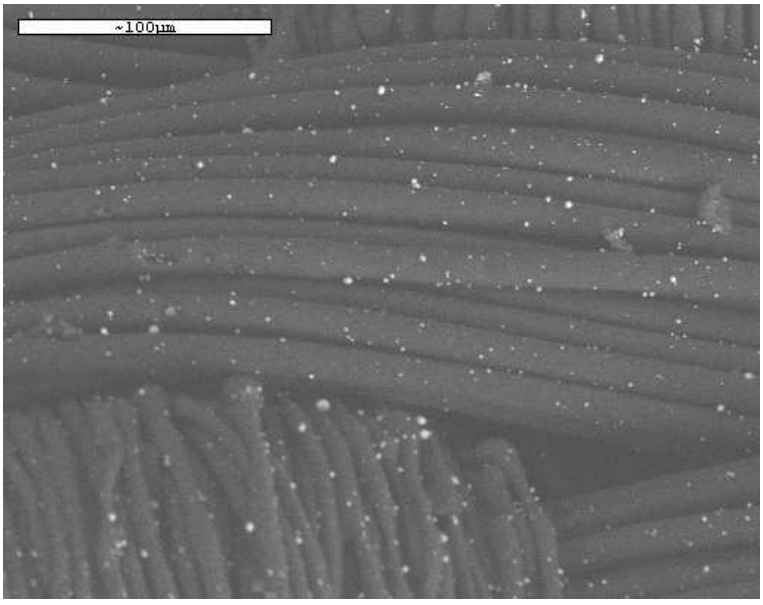

Figure 3.10: SEM image copper particulate on woven fabric from shot S788.

Table 3.6: Aluminum/copper button mass difference summary.

	Al,Cu Shot S789	Al,Cu Shot S791
Energy (kJ)	5.836	5.831
Sample Δm (mg)	−1091.1	−1130.8
Cathode Δm (mg)	−32.2	−29.2
	Δm (mg)	Δm (mg)
Button 1	−0.04750	0.10167
Button 2	−0.88333 (fabric)	0.20667
Button 3	0.47000	0.39667
Button 4	−5.84750 (PET)	0.25500
Button 5	0.51000	2.23250
Button 6	1.10667 (fabric)	0.51667
Button 7	0.56333	−1.49083
Button 8	0.97000	0.69083
Button 9	0.61667	0.45333
Button 10	0.81667	0.91333
Button 11	0.74333	–
Button 12	0.70333	–

and voltage traces for the mixed material shots are seen in Fig. 3.5.1. In Fig. 3.11(a), the long hold-off between the voltage and current pulses is an occasional feature of the discharge.

3.5.2 Particulate Observation

Significant particulate accumulation was observed in the mixed material shots. The SEM images shows particulate which appeared to have some of the splattering characteristic of the aluminum; however, there were differences between either of the images from single material shots and the mixed material shots. In addition to the features from molten aluminum, there were also large quantities of well-formed spherical particulate – characteristic of copper. SEM images from S789 for several buttons and magnifications are seen in Fig. 3.5.2. The EDX composition mapping showed that the particulate accumulated was a mixture of aluminum and copper. Figures 3.13 and 3.14 show maps for buttons 10 and 12. It is clear in these images that some of the particulate is composed of mostly one material, but the majority of the particulate contains both aluminum and copper. Table 3.7 presents the cumulative particle sizing results. On the average, it appears that the particle diameters are between those of the pure aluminum and copper cases.

3.5.3 Metals Comparison

For the different metal shots, a comparison was made of the average mass accumulation versus distance from the source exit. Fig. 3.15 shows this data. Only a slight increasing trend could be observed, so no definite conclusions can be drawn from this comparison. Another trend observed how the average particle diameter varied by material. As seen in Fig. 3.16, aluminum tended to have the largest particle

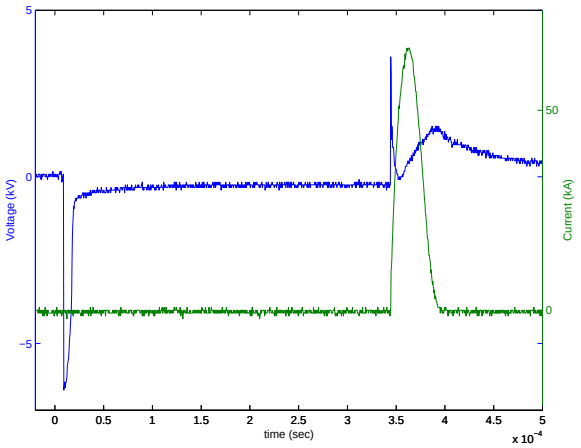

(a) S789

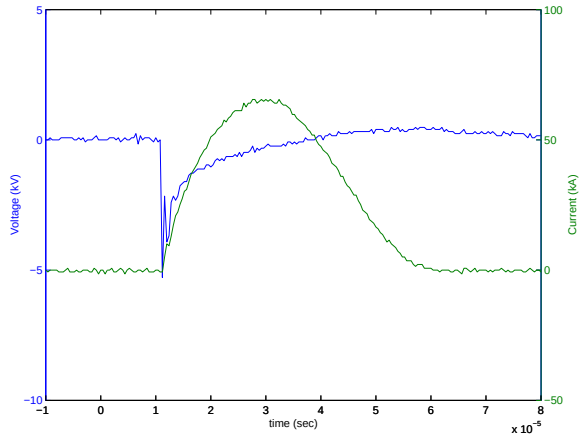

(b) S791

Figure 3.11: Plots of aluminum/copper shots sample current and voltage traces.

Table 3.7: Shot S789 Mixed Al/Cu particulate analysis summary.

Button	Axial Distance (cm)	Mag., # of images	$d_{15.9\%}\mu$m	$d_{50\%}\mu$m	$d_{84.1\%}\mu$m	GSD	R^2
1	12.7	overall, 3	0.21	0.48	1.06	2.22	0.956
3	31.75	overall, 3	0.45	0.93	1.94	2.08	0.975
5	31.75	overall, 3	0.42	0.86	1.73	2.02	0.993
7	50.8	overall, 3	0.40	0.72	1.29	1.80	0.877
8	50.8	overall, 3	0.36	0.71	1.44	2.01	0.975
9	69.9	overall, 3	0.30	0.61	1.23	2.01	0.817
10	69.9	overall, 3	0.36	0.80	1.74	2.18	0.942
12	endplate	overall, 3	0.50	1.36	3.66	2.70	0.945

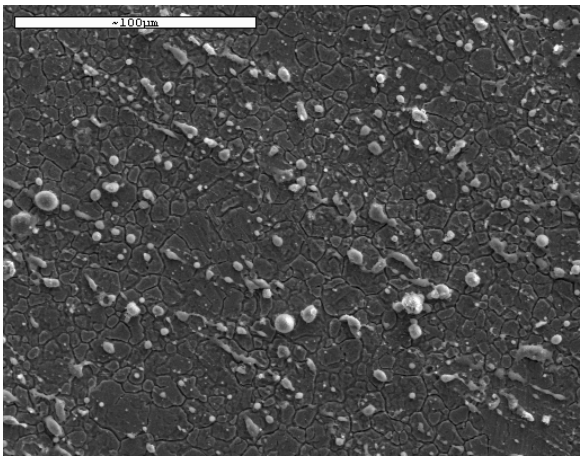

(a) Button 3, 500x

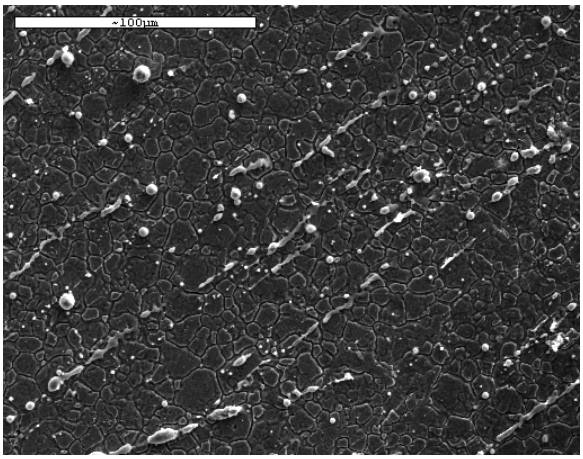

(b) Button 8, 500x

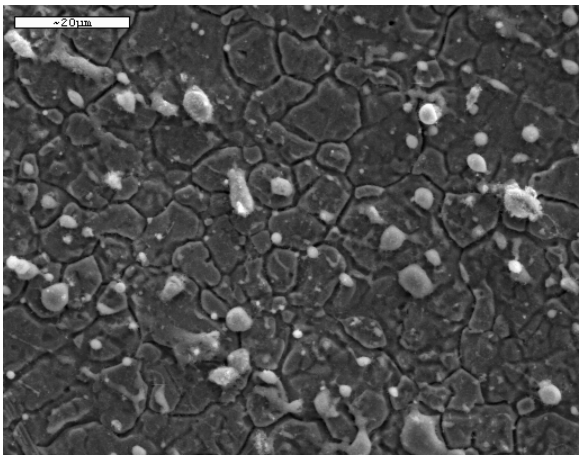

(c) Button 3, 1200x

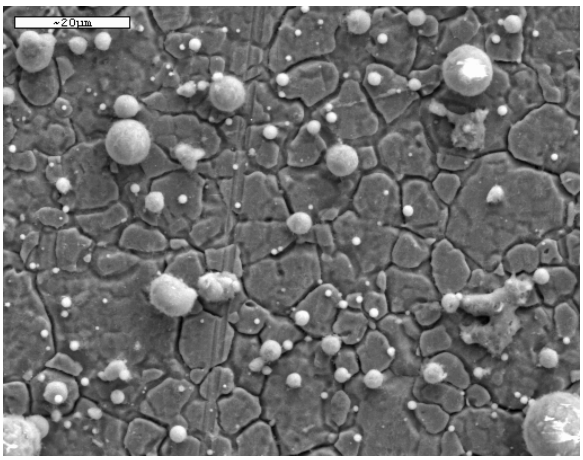

(d) Button 12, 1200x

Figure 3.12: SEM images of aluminum/copper particulate from shot S789.

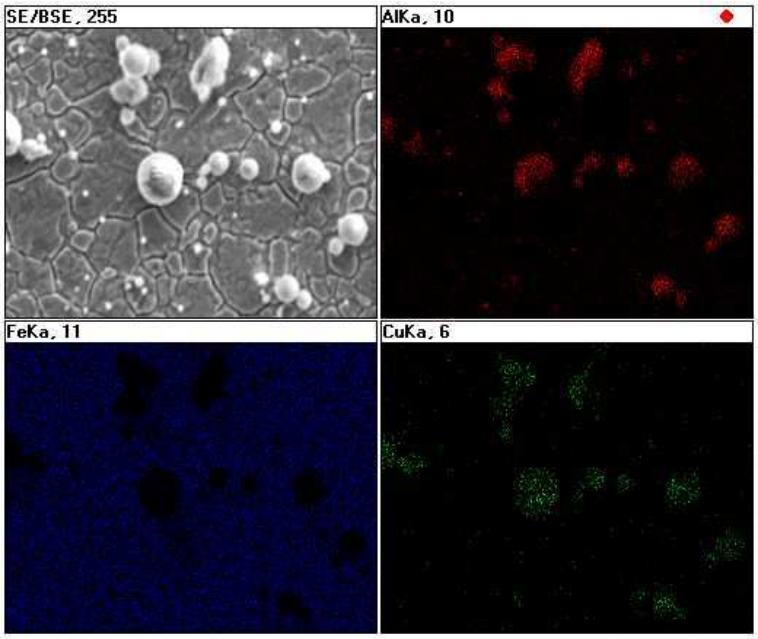

Figure 3.13: SEM image of aluminum/copper shot S789 EDX map of button 10.

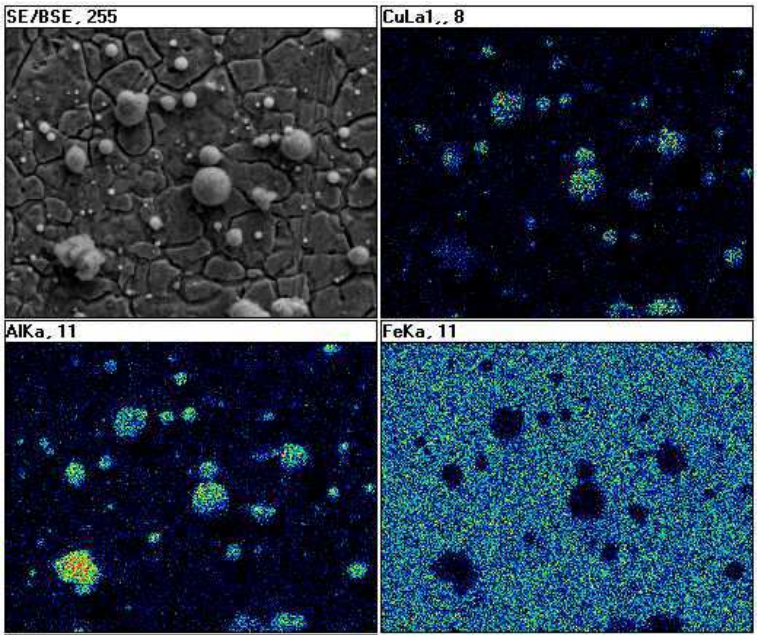

Figure 3.14: SEM image of Al/Cu shot S789 EDX map of Button 12.

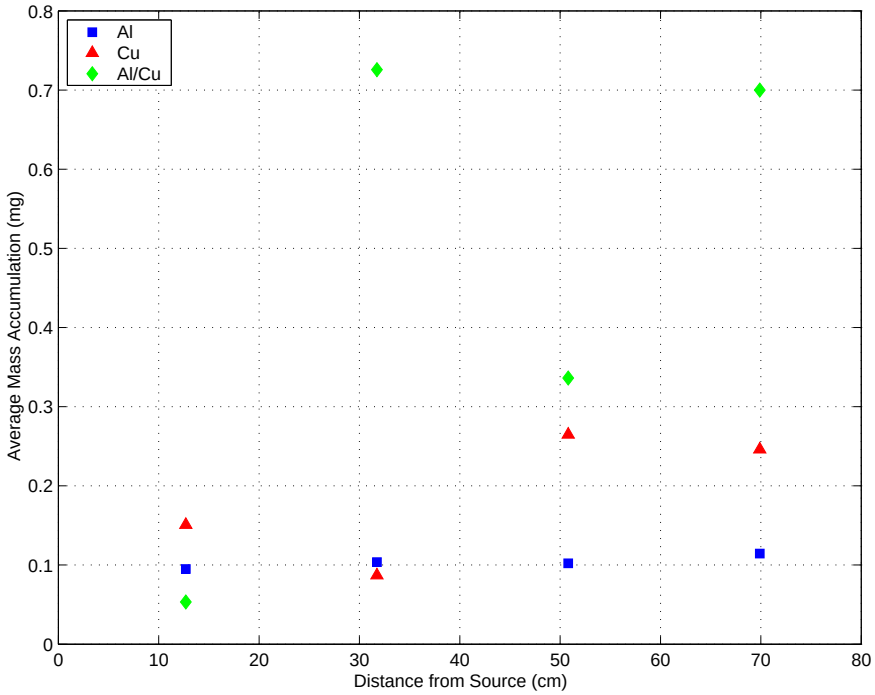

Figure 3.15: Comparison of average axial mass accumulation by sleeve material.

diameters, then the aluminum/copper mixture, and the smallest was the copper. Interesting to note in this plot is how the aluminum and mixed sleeve diameters follow roughly the same trend. These diameters were determined from the same magnifications and multiple images combined. The copper diameters follow a different trend and seem to be the smallest, except for the large jump at the third location. While the diameters measured for aluminum and mixed material particulate compare well, it is more difficult to justify the comparison with the copper particulate. What is needed are SEM images of copper particulate taken at the same magnifications as for the other materials.

3.6 Polycarbonate

3.6.1 Overview

Shots S783, S784, S792, S793 were all performed with Lexan sleeves. Shot S783 was performed as a diagnostic shot. Shot S784 was performed to collect particulate on copper, PET, and woven fabric covered buttons. Shots S792 and S793 were the first two unsuccessful optical spectroscopy tests. All 4 shots were taken at net input energies of 5.6-5.7 kJ. Current and voltage traces are seen in Fig. 3.6.1. The sleeve and button mass differences are summarized in Table 3.8 for the shots where these measurements were taken - after some of the Lexan shots the sleeves were irremovable from the insulators. From the buttons which showed mass gain after the shot, it is apparent that much less mass accumulated than

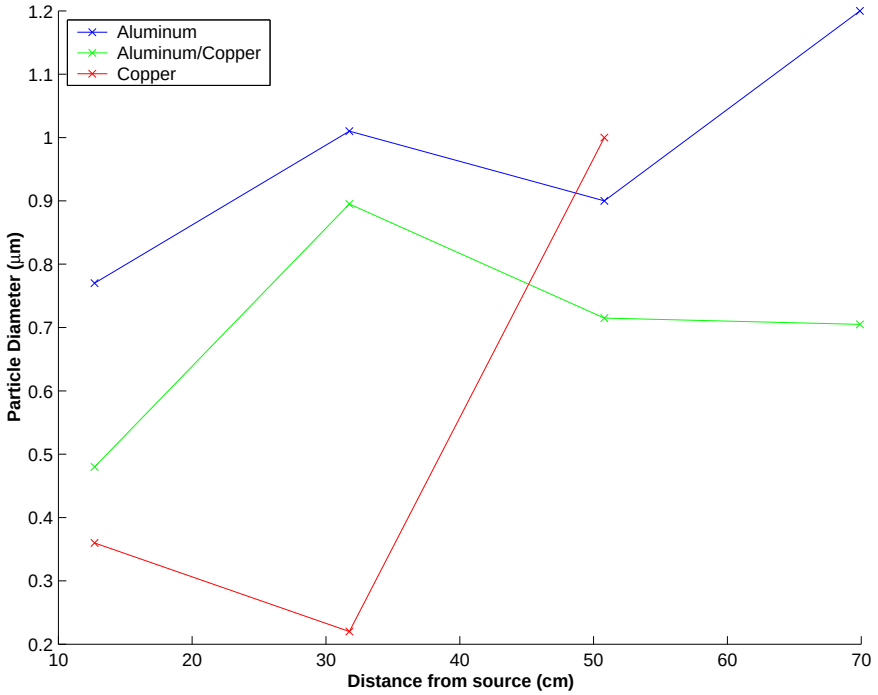

Figure 3.16: Comparison of $d_{50\%}$ by material.

for shots taken with metal sleeves.

3.6.2 Particulate Observation

The Figs. 3.18, 3.19, and 3.20, show the situation for the Lexan particulate gathered. No clearly discernible particulate was found on the copper substrate; however, the particulate accumulation on fabric is clear. Additionally, particulate remained after the washing test was performed. One noticeable feature in Fig. 3.18 is the damage to the substrate surface. This damage appears to be from particulate that impacted with the substrate surface. This button was located at the position closest to the source exit, as were the buttons exposed to different materials which also exhibited these features. Where the particulate was observed, the composition of the particulate is also unknown, because EDX returned no useful results on fabric. The elements that comprise the fabric and Lexan were not detectable with the available system. One concern with the images of the fabric is the apparent damage; there appears to be melting of the fabric. This damage could occur in the SEM. There are no blank images of the fabric before treatment to compare to, and it is likely that the blanks would be similarly damaged if the SEM was the source of the damage.

Very few of the micrographs contained countable particulate. The results from the small amount that was measured is seen in Table 3.9. Each image contained far less than 100 particles, which explains the poor quality of the distribution fits. The amount of countable particulate is hardly statistically

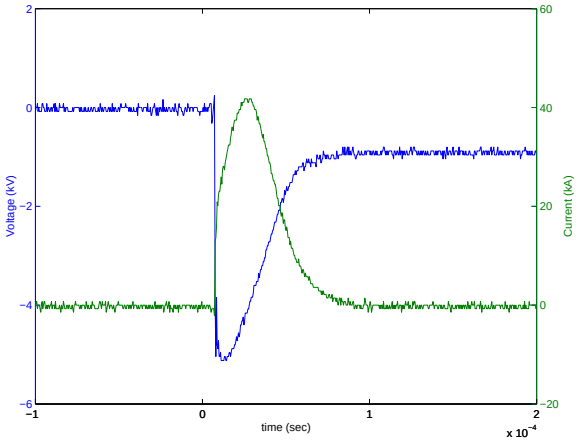

(a) S783

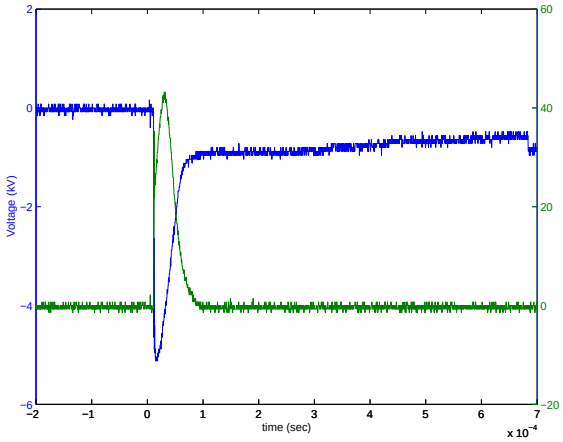

(b) S784

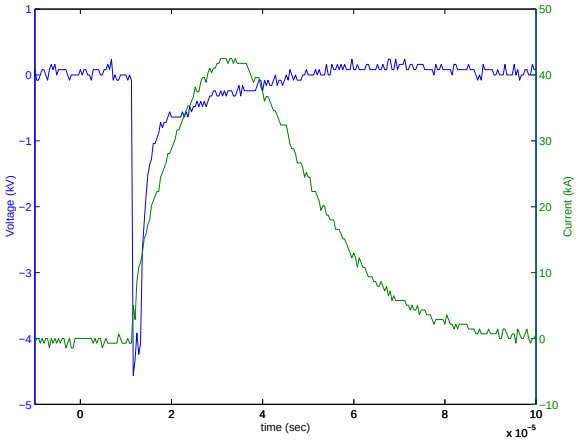

(c) S792

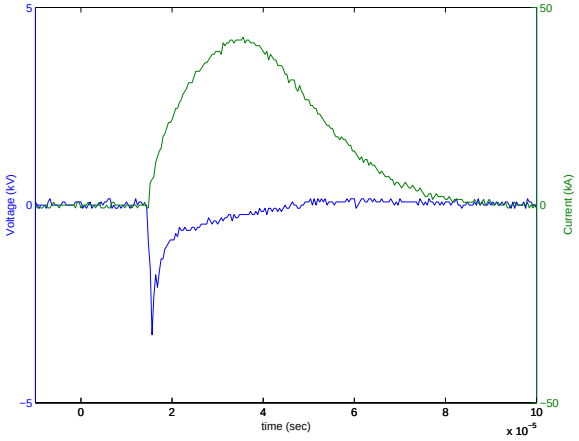

(d) S793

Figure 3.17: Plots of Lexan shots sample current and voltage traces.

Table 3.8: Lexan button mass difference summary.

	Lexan Shot S783	Lexan Shot S784
Energy (kJ)	5.616	5.725
Sample Δm (mg)	−530.72	−53.85
Cathode Δm (mg)	−77.2	−9.08
	Δm (mg)	Δm (mg)
Button 1	–	0.07667 (Cu)
Button 2	–	−0.34200 (PET)
Button 3	–	0.02667 (Cu)
Button 4	–	−0.00333 (fabric)
Button 5	–	0.05000 (Cu)
Button 6	–	−0.31667 (PET)
Button 7	–	−0.02000 (Cu)
Button 8	–	0.00333 (fabric)
Button 9	–	−0.08667 (fabric)
Button 10	–	−0.20667 (PET)
Button 11	–	0.06000 (Cu)

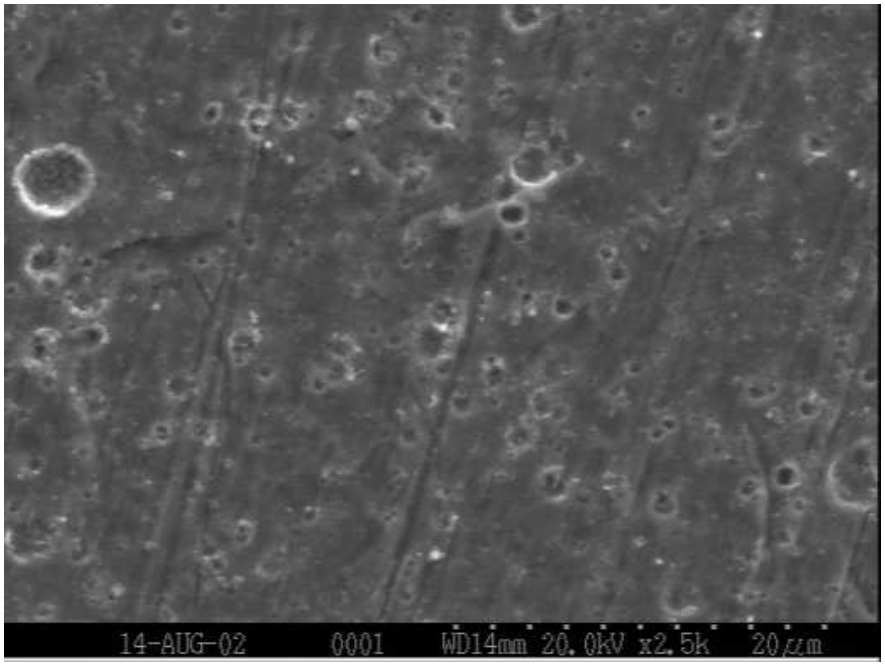

Figure 3.18: SEM image showing no Lexan particulate on a copper button from S784.

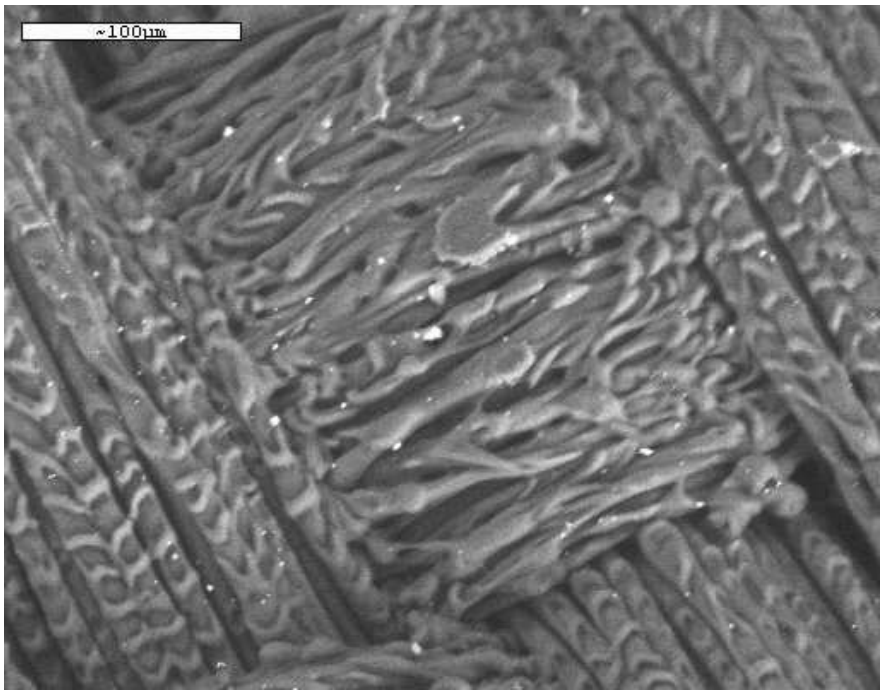

Figure 3.19: SEM image of Lexan particulate on unwashed woven fabric from S784.

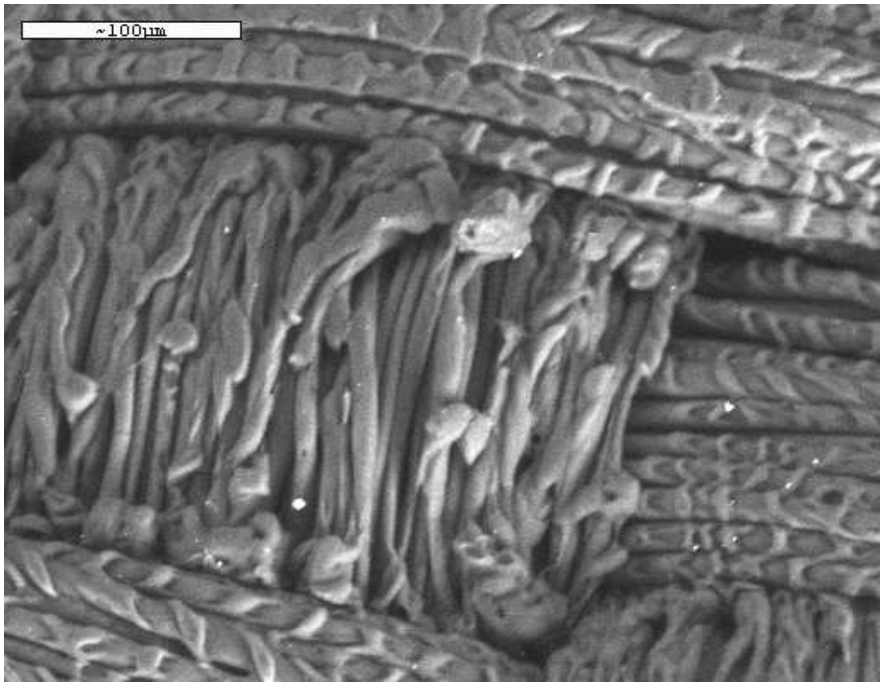

Figure 3.20: SEM image of Lexan particulate on washed woven fabric from S784.

Table 3.9: Shot S784 Lexan particulate analysis summary.

Button	Axial distance (cm)	Mag., # of images	$d_{15.9\%}\mu$m	$d_{50\%}\mu$m	$d_{84.1\%}\mu$m	GSD	R^2
4	31.75	3500x, 2	0.10	0.21	0.45	2.14	0.877
6	31.75	2000x, 1	0.13	0.26	0.49	1.88	0.416
9	50.8	800x, 1	0.29	0.58	1.14	1.97	0.581
u5	endplate	1000x, 1	0.31	0.73	1.72	2.36	0.984

significant, but computing the sizes does give a general idea that the particles are in the same range as for other materials.

3.7 Teflon

3.7.1 Overview

Teflon was a material of interest, because the fluorination of fabrics leads to a more hydrophobic fabric. Hydrophobic fabrics can last longer in environments where water damage over time is a factor. It was hoped that the plasma would dissociate the Teflon, and then the fluorine molecules or ions would implant into the exposed fabric surface. In a quick test of treated and untreated fabric, the fabric exposed to the Teflon plasma did appear more hydrophobic than the untreated plasma. However, the difficulty using Teflon capillaries in SIRENS meant no further tests were conducted.

Shots S786 and S787 were performed with Teflon liners. Shot S786 included copper and woven fabric covered buttons used to collect particulate. This was the first shot performed with the new Tektronix TDS2024 oscilloscope, and the default settings on the scope clipped the electrical diagnostic traces. So, shot S787 was performed to collect good diagnostic data. Both shots were taken at approximately 5.7kJ. Current and voltage traces from shot S787 are seen in Fig. 3.21. The Teflon sleeves could not be removed from the insulators after being fired with, so mass losses could not be obtained. The mass differences for the buttons used in S786 are seen in Table 3.10

3.7.2 Particulate Observation

Not only was Teflon the most difficult liner material to use, but also as with Lexan, only the fabric showed any particulate accumulation. When an individual particles was analyzed with EDX, the particle appeared to be largely iron in composition. The iron is material from the cathode. Some fluorine appeared in the maps, but because of its low atomic number, it was difficult to detect with the available EDS system. Because only individual particles could be mapped with EDX, it is impossible to know the overall composition of the particulate.

While particulate did accumulate on the fabric, there was also significant damage to the fabric - in the form of broken fibers which are readily apparent in the micrograph seen in Fig. 3.22. The fabric

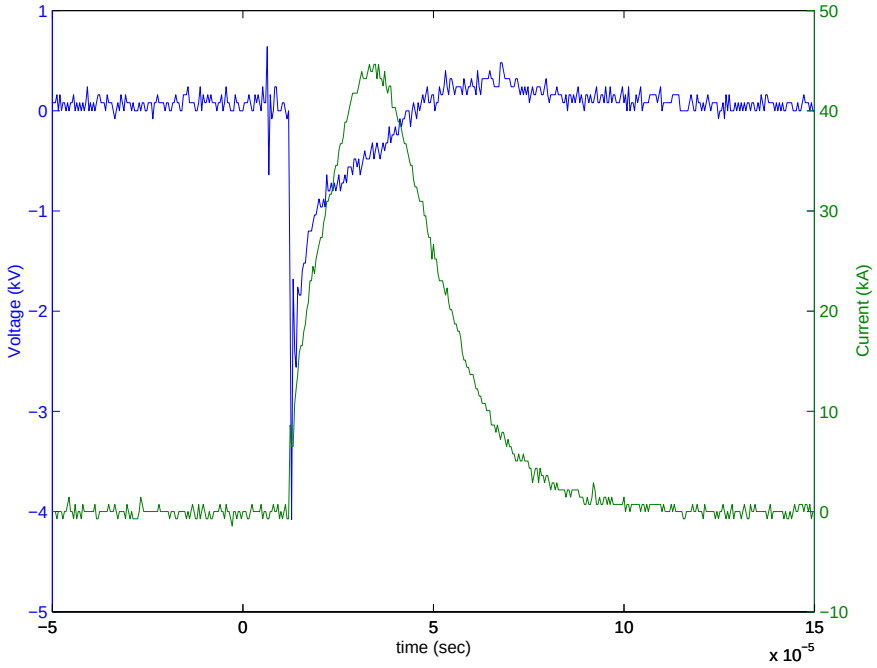

Figure 3.21: Teflon shot S787 current and voltage traces.

Table 3.10: Teflon shot S786 button mass difference summary.

	Teflon Shot S786
Energy (kJ)	5.714
Sample Δm (mg)	–
Cathode Δm (mg)	−47.22
	Δm (mg)
Button 1	0.08333 (Cu)
Button 2	−0.03667 (fabric)
Button 3	0.10333 (Cu)
Button 4	0.07667 (Cu)
Button 5	−0.15000 (fabric)
Button 6	−0.05667 (fabric)
Button 7	0.00000 (fabric)
Button 8	0.14750 (Cu)
Button 9	−0.09000 (fabric)
Button 10	0.05333 (Cu)
Button 11	−0.03833 (Cu)
Button 12	−0.01333 (Cu)
Button 13	0.00667 (Cu)
Endplate	51.34167

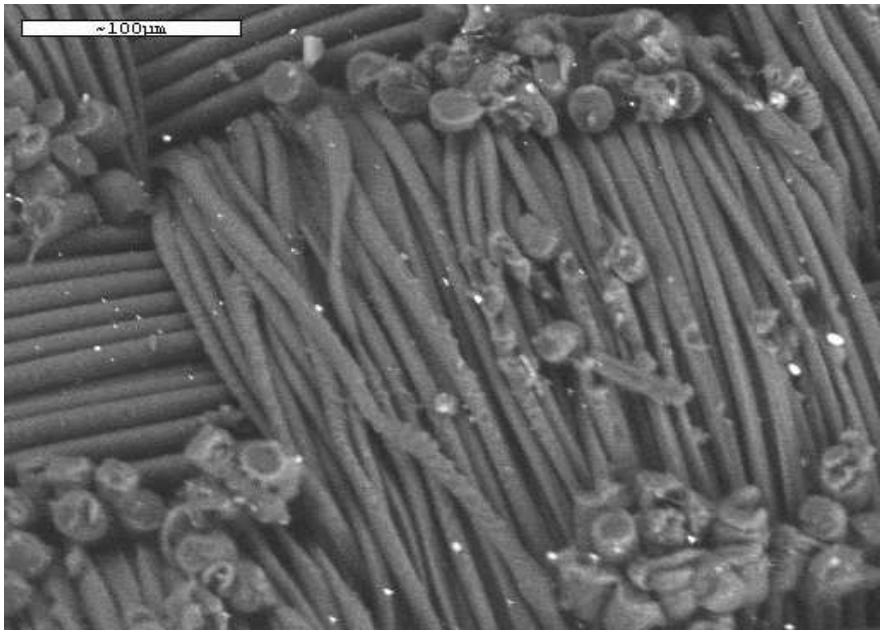

Figure 3.22: SEM image of unwashed fabric exposed to Teflon plasma in shot S786.

was damaged some in the initial washing process before being fired upon, but it is also possible that the plasma exposure further damaged the surface. Also interesting to note about the fabric is that the loose fibers and broken ends were removed by the washing process so that the fabric in Fig. 3.23 does not appear damaged.

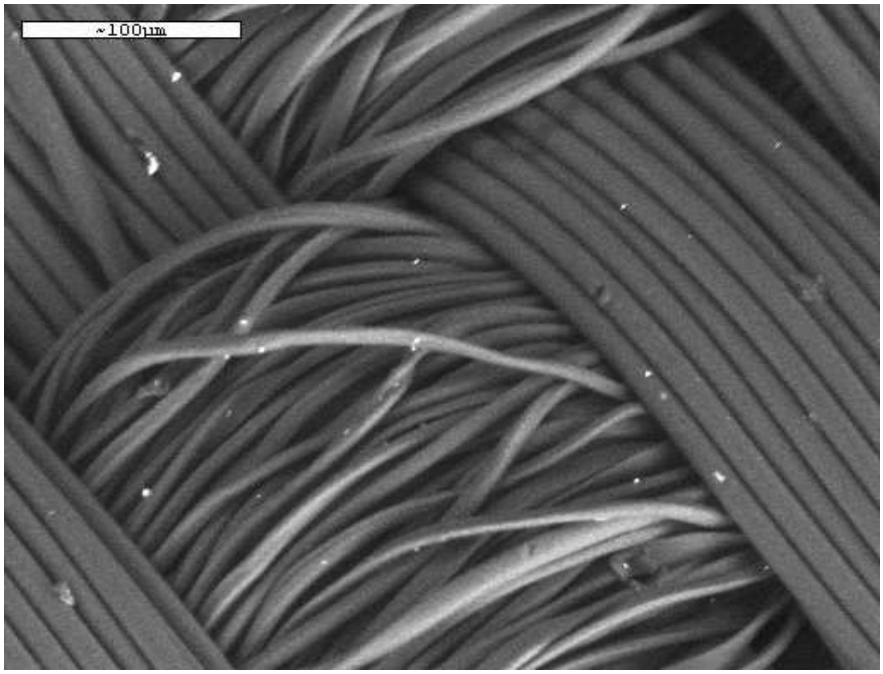

Figure 3.23: SEM image of washed fabric exposed to Teflon plasma in shot S786.

Chapter 4

Spectroscopic Measurements

For the three main types of sleeves used - aluminum, copper, and Lexan, spectroscopic measurements were taken at approximately 7, 32, 47, and 68cm from the source exit (±1cm for each position). The first measurement was as close to the source as was convenient with the fiber, while the other three positions correspond to positions at which particulate was collected. At each location, 50μm fiber was attached to either the barrel exit, the glass expansion chamber, or the glass chamber guides so that the fiber end was parallel to the plasma flow and the fiber end was at the approximate radial position of a button. The orientation of the fiber meant that the spectra obtained close to the source were for the outer edge of the plasma and not the plasma core. In previous studies such as [11], the optically thick boundary layer interfered with the observation of certain lines. The plasma was therefore viewed on-axis to avoid the boundary layer. This problem did not interfere in the present work, so the fiber orientation was kept perpendicular to the source axis.

The small fiber probe was attached to a 400μm patch cord through a variable attenuator. The attenuation needed ranged from approximately 50% close to the source to none at all for Lexan shots far from the source. The use of the fiber probe was very convenient, because the fiber exposed to the plasma quickly become dirty and brittle. Between shots, the fiber was visually inspected to determine if some portion of the fiber end needed to be removed. Even though the 50μm fiber was very difficult to handle, the brightness of the plasma source necessitated its use, and the use of a variable attenuator. A hardware trigger for the HR2000 spectrometer was taken from the delay generator, and the automatic integration time of 50msec in the OOIBase32 controlling software was acceptable because the spectra were time-integrated over the length of the discharge.

For the density measurements in a dense plasma, such as electrothermal plasmas, the typical H_β Balmer line can be difficult to measure broadening from, so the H_α line is used instead [22]. Specifically, the H_β is useful when the electron density of the plasma is approximately 10^{15} to $3(10)^{17}$ cm^{-3} while the H_α line is useful up to densities of approximately 10^{19} cm^{-3}. In the SIRENS plasma the density is

approximately in the H_β range, but it is convolved with other lines and therefore more difficult to use. The other main assumption necessary for the use of the H_α line is that radiative transfer effects can be allowed for in this type of dense plasma [25]. The H_α line was observed in each type of plasma due to the presence of at least a small section of Lexan in the source section. However, at distances further from the source, the line was not apparent, so the density measurement had to be taken using other lines, such as the neutral copper lines also used to calculate temperature. So, to compare the two density calculations, densities from both types of lines were calculated whenever the lines were distinguishable enough to fit with a Lorentzian function. The full methodology behind the density calculations was discussed previously in Chapter 2.

To confirm that Doppler broadening was a negligible effect on the line width, the relation from [28] was used to estimate Doppler broadening. This relation assumes LTE so that the velocity distribution can be approximated as Maxwellian, resulting in a Doppler width of:

$$w_D = 7.16(10)^{-7}\lambda\left(\frac{T_g}{M}\right)^{1/2} \quad (nm). \tag{4.1}$$

Using values for the Hα line of: $\lambda = 656.3$nm, emitter temperature $T_g = 0.5$eV, and emitter mass M=1 amu, the resulting width of 0.04nm is well below the spectrometer resolution and definitely a negligible effect.

4.1 Aluminum

In addition to temperature and density measurements, the progression of the spectra with distance from the source is a qualitative way to analyze the plasma. As seen in Fig. 4.1, there is a slight blackbody shape to the background. At the locations further from the source, the blackbody features are markedly less so that the background appears almost constant. Another noticeable feature is the decrease in the relative magnitude of the H_α line. This indicates that recombination is taking place and that further downstream the plasma in more like a neutral aluminum gas [33].

4.1.1 Temperature

Spectra were acquired for shots 799, 802, 806, and 808. In shot S799, the temperature was calculated using the relative intensities of single ionized aluminum lines ands data from [31]. Compared to the spectra acquired at the other three positions the copper lines were weak, and therefore not used to calculate the temperature in the spectra acquired at the position closest to the source exit. The lines and relevant data are summarized in Table 4.1. For the other three aluminum shots, the aluminum lines were either too weak or too convolved with other species to accurately determine their intensities. Instead, the neutral copper lines were used, as seen in Table 4.2. These lines appear because of the

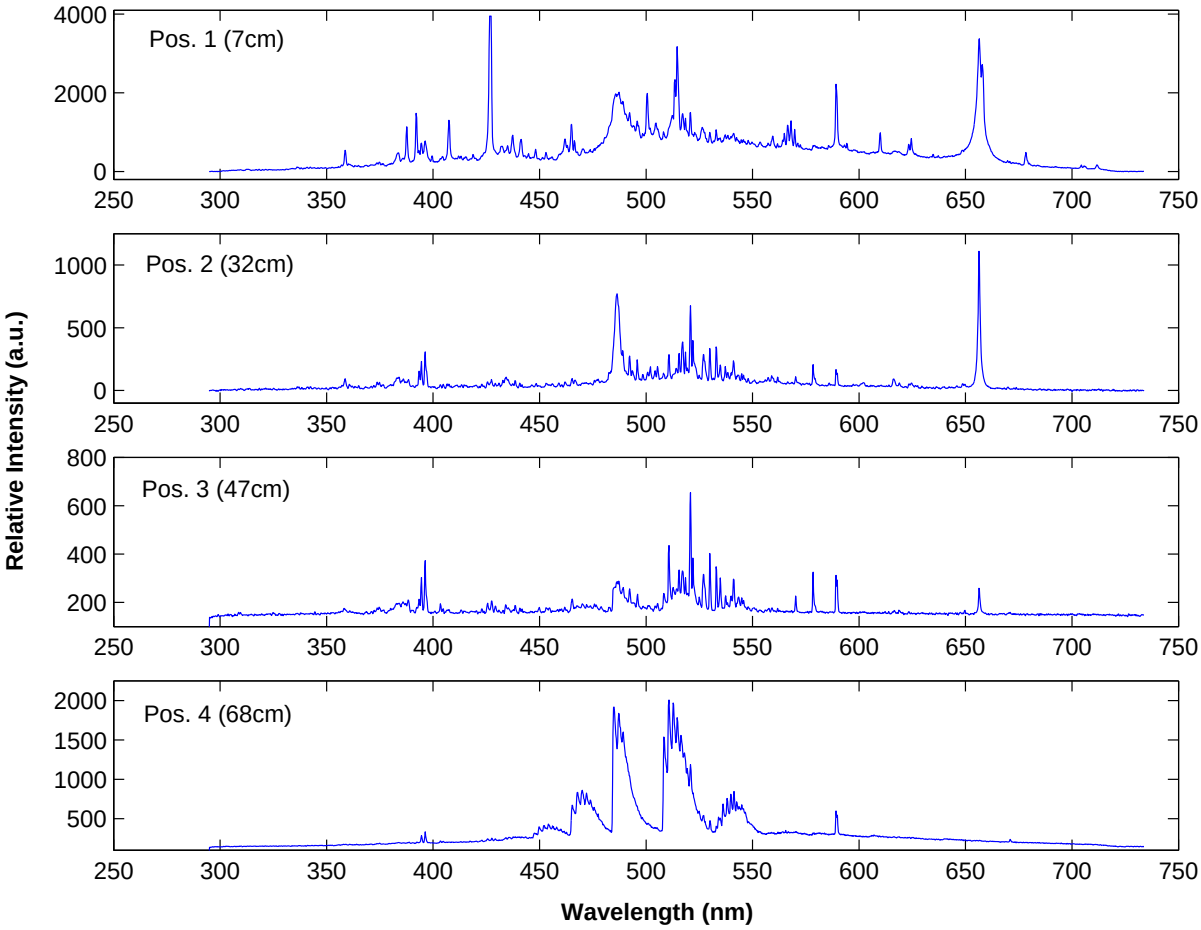

Figure 4.1: Spectra acquired for aluminum shots S799, 802, 806, and 808 (positions 1, 2, 3, and 4 respectively)

Table 4.1: Aluminum shot S799 single ionized aluminum reference lines.

Species	Line (nm)	E_u (eV)	g_u	A (10^8 sec^{-1})	Intensity
Al II	466.3	13.25659	3	0.53	785
Al II	559.31	15.47257	5	2.3	898
Al II	623.31	15.06218	5	0.84	691
Al II	624.55	15.06218	7	1.1	838

Table 4.2: Aluminum shots S802, S806, S808 neutral copper reference lines.

Species	Line (nm)	E_u (eV)	gA (10^8 sec^{-1}	S802 Intensity	S806 Intensity	S808 Intensity
Cu I	510.554	2.65	0.051	286	435	1860
Cu I	515.324	4.30	4.7	296	334	1643
Cu I	521.820	4.30	5.8	398	383	-
Cu I	529.250	5.38	3.2	335	402	328
Cu I	570.020	2.65	0.014	110	226	-
Cu I	578.213	2.63	0.054	206	345	-

copper content in the cathode. The apparent decrease in the singly ionized aluminum lines in the spectra obtained further from the source likely indicates recombination taking place as the plasma expands away from the source.

To calculate the temperature, a choice had to be made concerning the source of the data used in the relative line method. The values of the atomic transition probabilities can differ greatly depending on the data source. A comparison of the temperature calculated from neutral copper lines was made in [23] using the two main data tables - [34] and [35]. It was shown that the data from [34] resulted in higher temperatures than when using [35]. The same trend was found in the present work using the parameters from each and the relative line intensities measured. In addition, the study found that the reliability of the experimental data was better with the data from [35]. Therefore, only the results using the parameters from [35] will be presented. However, Table 4.3 presents the alternate values from [34] for the neutral copper lines for reference.

As seen in Fig. 4.2, the temperatures returned from the copper lines was approximately 0.5eV for the three furthest locations. The aluminum lines returned a much higher temperature of 1.5eV closest to the source. All lines provided fairly good linear fits - a good validation for the LTE assumption. The

Table 4.3: Alternate neutral copper reference lines from [34].

Species	Emission Line (nm)	g_u	E_u (eV)	A 10^8 (sec^{-1})
Cu (I)	510.6	4	3.82	0.020
Cu (I)	515.3	4	6.19	0.60
Cu (I)	521.8	6	6.19	0.75
Cu (I)	529.3	4	7.74	0.15
Cu (I)	570.0	4	3.82	0.109
Cu (I)	578.2	2	3.79	0.0165

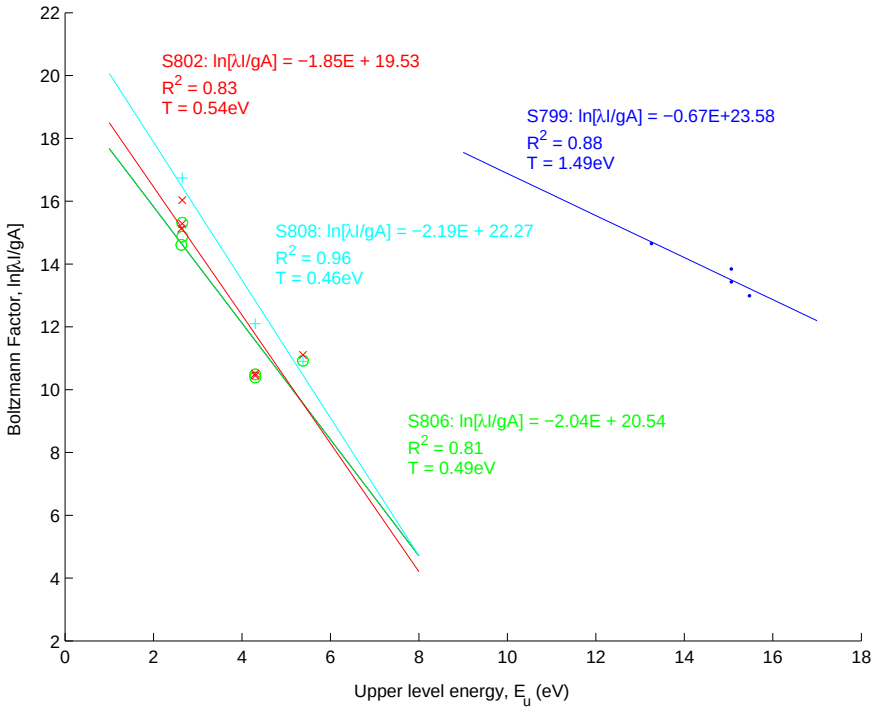

Figure 4.2: Boltzmann plot for aluminum shots S799, 802, 806, and 808 for temperature measurement, using aluminum and copper lines.

uncertainty in the plasma temperatures is not shown in Fig. 4.2, but it is significant for the relative method. Based on the uncertainty in the data from [35], the uncertainty in the temperature calculated from the singly ionized aluminum lines is estimated to be ±50%, but only ±25% for the neutral copper lines. Therefore the temperature of 1.5 ± 0.75eV for S799 is less reliable than the 0.5 ± 0.125eV.

4.1.2 Density

As seen in Table 4.4, the density was calculated using the Stark broadening of the Hα line and the broadening of the neutral copper lines when possible. For the copper lines, the density was taken to be the average of all the line densities. Appendix C presents a table with the individual line densities calculated, as well as densities calculated from the H_α line using alternate methods. In Table 4.4, the densities calculated from the H_α broadening follow the expected decreasing trend with increasing distance from the source. The densities found using the copper lines are not only slightly higher, they also do not follow the same decreasing trend. For both methods, the uncertainty in the density is in the 20-30% range.

Table 4.4: Aluminum shot plasma density, as a function of distance from source.

Shot No.	Axial Distance (cm)	n_e (m^{-3}) (Hα)	n_e (m^{-3}) (Cu I)
799	7	$3.32(10)^{23}$	-
802	13	$7.95(10)^{22}$	$3.39(10)^{23}$
806	47	$1.45(10)^{22}$	$3.85(10)^{23}$
808	68	-	$1.64(10)^{24}$

4.2 Copper

Spectra were acquired for copper shots 800, 801, 805, and 809 at increasing distances from the source exit. As with the aluminum spectra, the copper spectra, seen in Fig. 4.3, also show the initial blackbody (or greybody) background, characteristic of the plasma close to the source. Further from the source, the spectra shows a shape that was seen with all three liner materials. The spectra acquired furthest from the source are much more convolved. This is another indication that recombination is taking place.

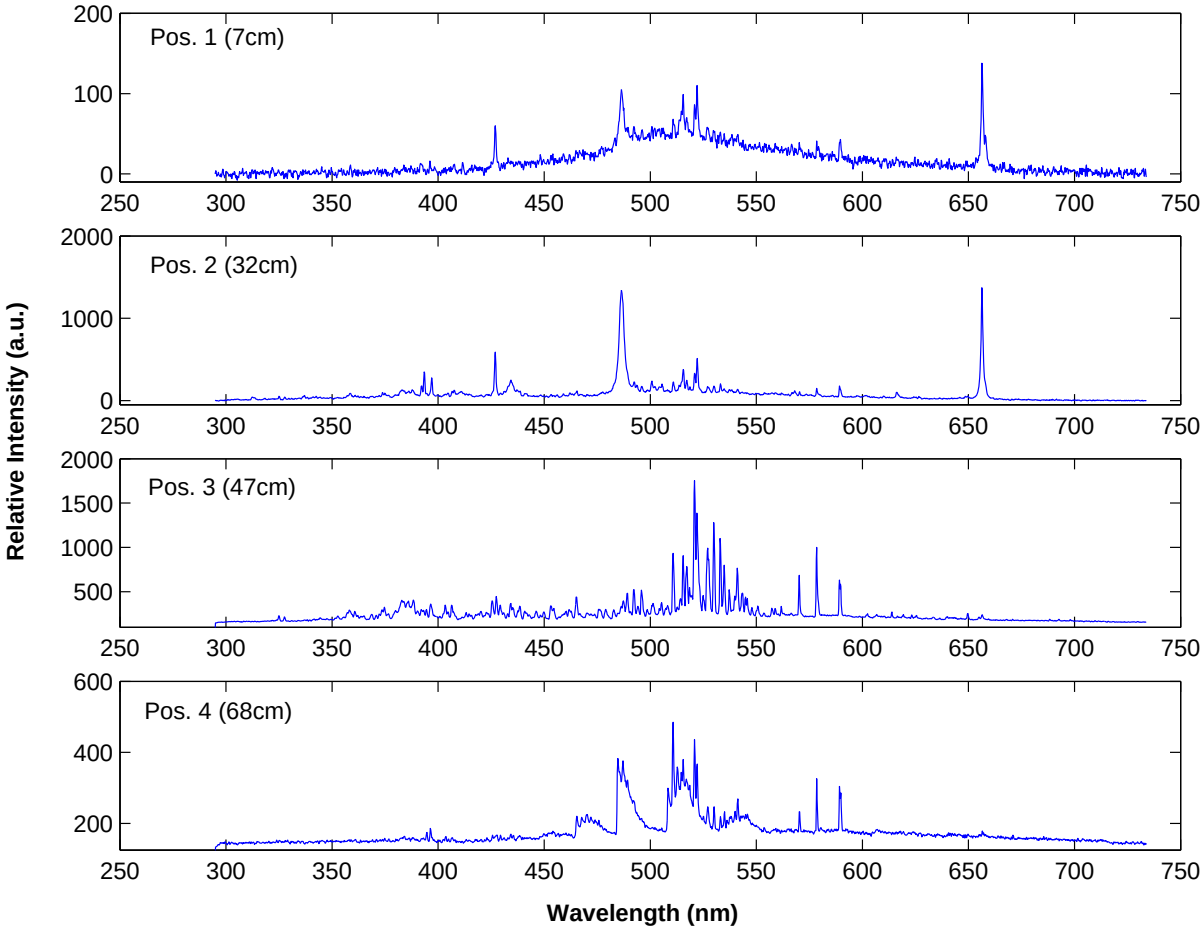

Figure 4.3: Spectra acquired for copper shots S800, 801, 805, and 809 (positions 1, 2, 3, and 4 respectively).

4.2.1 Temperature

As expected in the copper plasmas, the neutral copper lines were very clear, so the temperatures were calculated from these lines. The copper sleeve, in addition to the copper content of the cathode contributed to the appearance of these lines. Figure 4.4 shows the calculated temperatures, and the linearity — confirming the LTE assumption. As with aluminum, all of the temperatures are approximately 0.5eV, including the temperature closest to the source. All of the copper and aluminum spectra shots were taken at input energies of approximately 5.8kJ, so it is not too surprising that the temperatures could be the same.

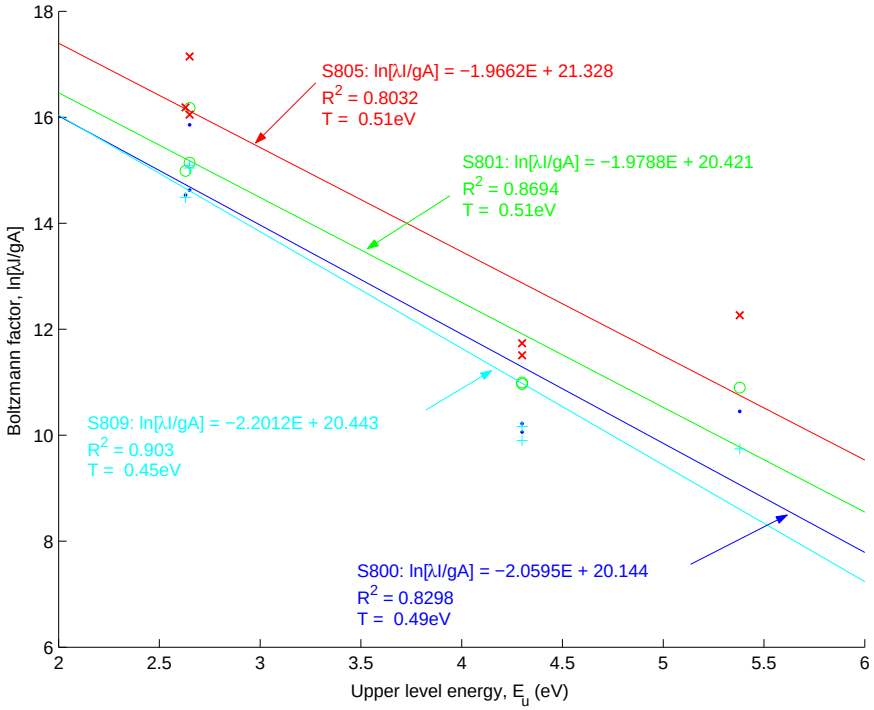

Figure 4.4: Boltzmann plot for copper shots S800, 801, 805, and 809 for temperature measurement, using copper lines

4.2.2 Density

In the spectra recorded at the two closest locations, the Hα line is very clear. At the third location, the Hα line is small, but the density was still able to be calculated from its Stark broadening. At the location furthest from the source, the density could only be calculated from the broadening of the neutral copper lines. All of the calculated densities are presented in Table 4.5. As with the aluminum shots, the densities from the copper lines are slightly higher than the densities from the H_α lines. However, the H_α densities in these shots are approximately constant, not following the expected decreasing trend. Instead, the densities from the copper lines show a somewhat decreasing trend. The three farthest copper

line densities are within uncertainty of each other, making the density appear constant after dropping off from the location closest to the source.

Table 4.5: Copper plasma density as a function of distance from source.

Shot No.	Axial Distance (cm)	n_e (m^{-3}) (Hα)	n_e (m^{-3}) (Cu I)
800	7	$4.62(10)^{22}$	$1.24(10)^{24}$
801	13	$5.91(10)^{22}$	$3.47(10)^{23}$
805	47	$3.32(10)^{22}$	$4.70(10)^{23}$
809	68	-	$5.19(10)^{23}$

4.3 Lexan

Spectra were acquired for Lexan shots 798, 803, 804, 807, and 810 at increasing distances from the source exit. Too much attenuation was used in shot 804 at the third location, so the spectrum was reacquired in shot 810. As with the aluminum and copper spectra, the Lexan spectra, seen in Fig. 4.5, also show the same blackbody characteristic of the plasma close to the source. Further from the source, the spectrum shows the same highly convolved shape that was seen with the other two liner materials. Notice in Fig. 4.5 that the H_α line is very clear at even the location furthest from the source. The much larger quantity of Lexan in the source produced much clearer hydrogen lines.

4.3.1 Temperature

As with the other liner materials, the neutral copper lines were apparent in the Lexan spectra. Therefore, the temperature was calculated from these lines. The Boltzmann plot, in Fig. 4.6, shows the temperatures calculated. Again, all of the temperatures are approximately 0.5eV, and do not appear to change with distance from the source exit. At 5.7kJ, the input energies for the Lexan shots were slightly lower than the metal sleeve shots, but this small difference did not appear to make a difference in the plasma temperature. Also, the linear fits are reasonable, confirming the LTE assumption.

4.3.2 Density

The Hα line was present in the polycarbonate spectra at each axial distance. From these lines, the plasma densities were calculated, as summarized in Table 4.6. Additionally, the densities were calculated from neutral copper lines for all but the closest spectrum. The trend of higher densities from copper lines again holds true in Lexan spectra. Also, the decreasing trend in density with axial distance is most clear Lexan densities from H_α lines. The densities from the copper lines do not appear to follow any clear trend with distance.

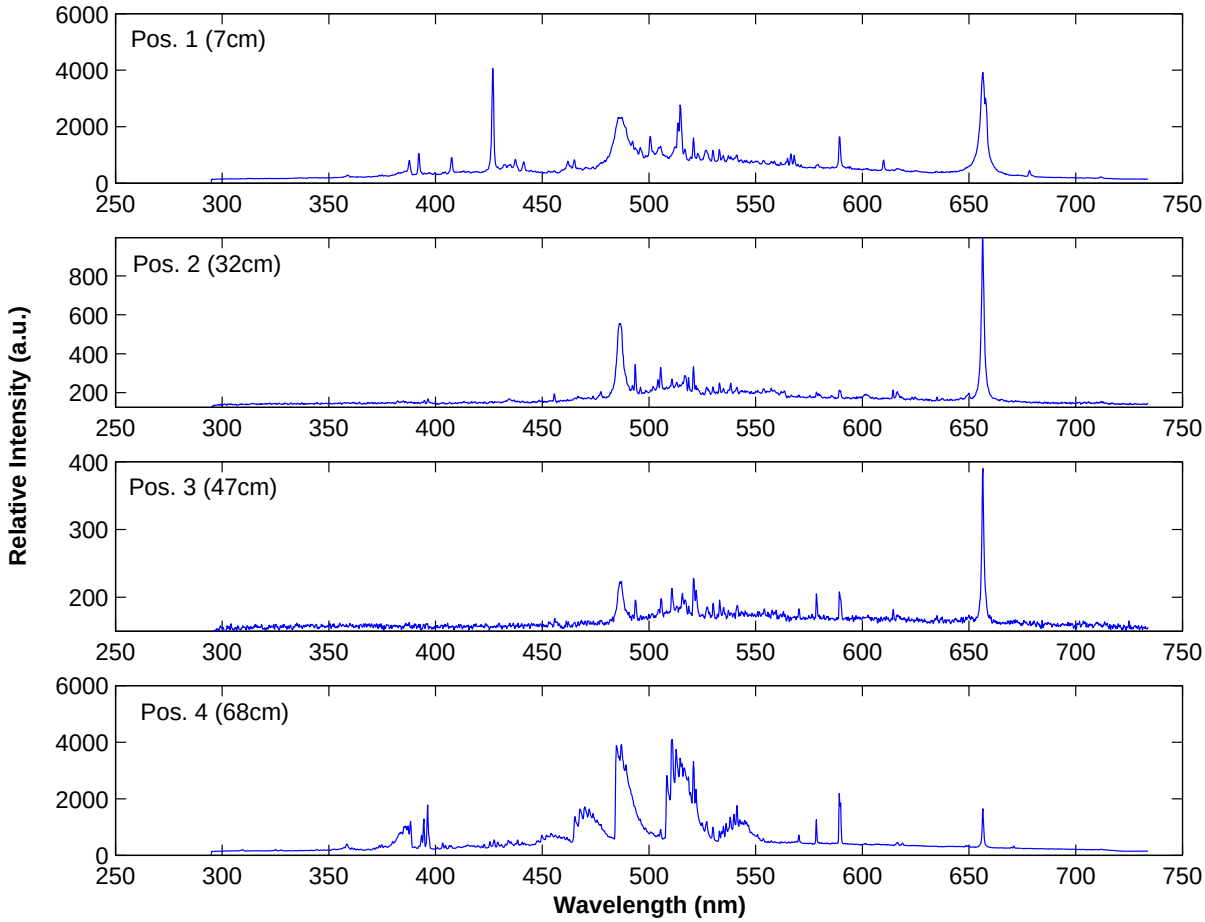

Figure 4.5: Spectra acquired for Lexan shots S798, 803, 810, and 807 (positions 1, 2, 3, and 4 respectively).

Table 4.6: Lexan plasma density as a function of distance from source.

Shot No.	Axial Distance (cm)	n_e (m^{-3}) (Hα)	n_e (m^{-3}) (Cu I)
798	7	$3.79(10)^{23}$	-
803	13	$1.23(10)^{23}$	$1.23(10)^{23}$
810	47	$4.53(10)^{22}$	$5.64(10)^{23}$
807	68	$1.52(10)^{22}$	$1.93(10)^{23}$

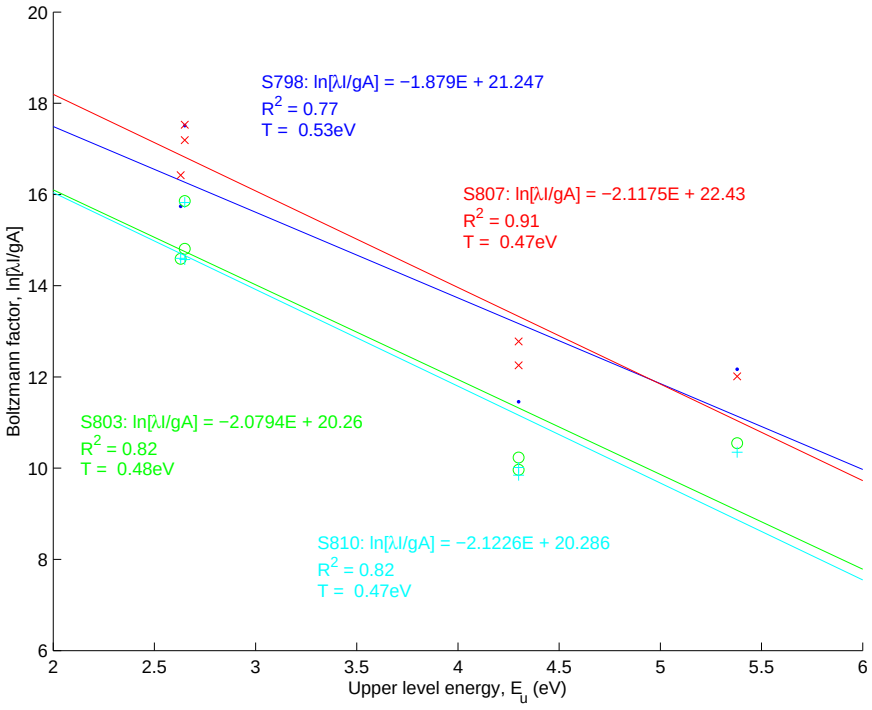

Figure 4.6: Boltzmann plot for Lexan shots S798, 803, 807, and 810 for temperature measurement, using copper lines.

Chapter 5

Plasma Parameter Scaling

Many previous studies have modelled electrothermal plasma sources or ablation controlled arcs. These models range from simplified semi-analytical solutions such as [36] to the much more complex computational model contained in [8]. Each study also has a different aim; the two listed above consider topics as different as average cross-sections and particle sizes, respectively.

Computational models tend to include the non-idealities of the electrothermal plasma, and require a code to obtain results. The aim of the present work was to simplify the ablation model of the plasma so that estimates to compare with experimental measurements of density and temperature would be simple to obtain. The expectation is not that the results will match the parameters obtained with diagnostic methods, but that the method will provide an easy way to quickly obtain estimates of plasma parameters in the low temperature, high density regime [33]. That is, the results from the estimations are not expected to predict the measurement. They are meant simply to verify the assumptions used to obtain results from experimental measurements.

Compared to the measurement of the discharge's electrical characteristics, measuring the light emitted is a complex task. From the easily obtained experimental measurement of voltage, current, and mass loss, both the density and temperature are estimated. These estimates lead to the validation of many of the assumptions used to further analyze the plasma – such as the blackbody assumption, and LTE. The arc plasma generated in the source section is in LTE because of the high pressures in the capillary due to the ablation of the liner. Therefore, the energy transfer mechanism to the capillary wall is radiation and the plasma surface radiates as a blackbody [8]. As discussed in the previous chapter, the plasma must be in LTE for the temperature calculations from spectra to be valid. Basing the estimates on the blackbody and LTE assumptions is considered reasonable because of the partial blackbody, or graybody, shape observed in the continuum shape of the acquired spectra.

To obtain simple estimates, several key assumptions will be made. For instance, although the plasma is not purely resistive, evident by the voltage leading the current in all of the current and voltage traces,

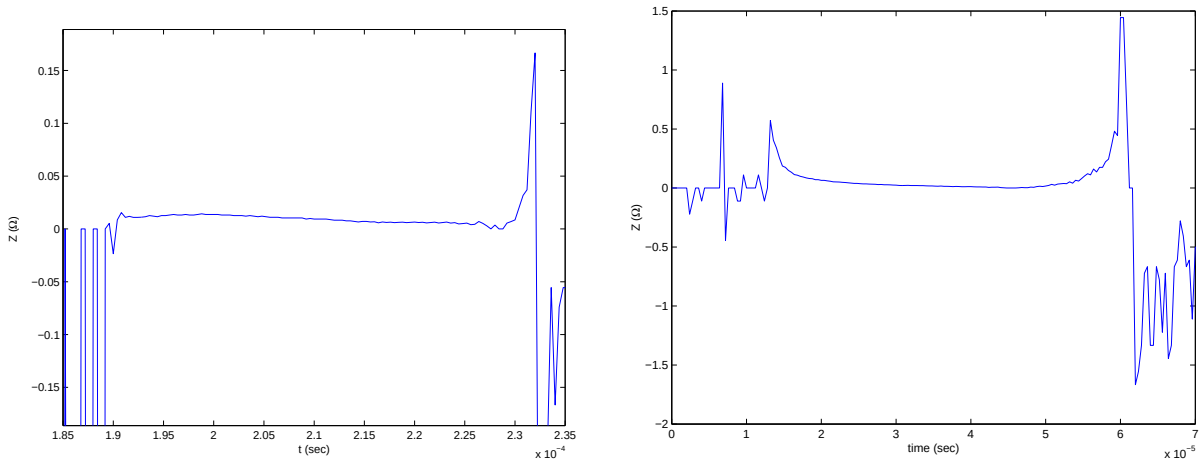

(a) S782 (b) S788

Figure 5.1: Plots of impedance versus time.

it can be approximated as such during the length of the discharge. This approximation is reasonable because typical impedance ($Z = V/I$) graphs, seen in Fig. 5 show that the plasma impedance is small and approximately constant when the current is flowing. Another key assumption is that the plasma is dominated by electron-neutral interactions, rather than electron-ion interactions. This will be discussed further in the "Average Density Calculations" section, where the assumption is used to simplify the equations.

5.1 Average Temperature Calculations

To approximate the average temperature of the plasma, a simple plasma ablation model was used. In this model, the plasma is controlled by the wall material ablation, where the input of electrical energy into the system leads to the heating of the weakly ionized plasma. Radiation from the heated plasma ablates the wall material. This ablated material increases the plasma density and becomes a vapor shield which prevents further radiation from reaching the wall and ablating the wall material further. Then, due to the pressure increase inside the capillary, the plasma is transported axially which leads to particle and convective energy loss of the plasma because the ablated material comprising the plasma is the energy carriers of the system [36]. In other words, the ablation rate depends on the radiation as:

$$\dot{n}_{abl} = \frac{2q''}{rH_{abl}}, \tag{5.1}$$

where the ablation energy, H_{abl}, is taken as the sublimation energy in this approximation. Another approximation is made here, where the sublimation energy is taken for the material of interest, though

the sleeve may consist several components. Since only time-integrated averages over the length of the discharge can be estimated from available mass loss measurements, the surface heat flux, q'' is investigated.

Based on previous research, an adjusted blackbody radiation model was used to represent the radiation of the plasma through the vapor shield [6]. This simple model allows for the temperature to be approximated from:

$$q'' = f\sigma_s T^4, \tag{5.2}$$

where q'' is the heat flux reaching the wall surface, σ_s is the Stephan-Boltzmann constant, T is the average bulk plasma temperature, and f is the fraction of the blackbody radiation emitted from the plasma through the vapor shield. Since only a fraction of the incident energy is transmitted through the vapor shield, the f factor must be included in the blackbody equation. Based on the experimental and computational results found in the past, the value of f was chosen as 10%, or 0.1, though the range spans 3-50% depending on the input energy into the plasma [6]. This model also assumes that the plasma temperature is much greater than the capillary wall temperature , $T^4 \gg T_w^4$. Additionally, the heat flux can be calculated from the mass ablated from the capillary as:

$$q'' = \rho H_{sub} \Delta x, \tag{5.3}$$

where ρ is the material density, H_{sub} the sublimation energy, and Δx the ablation depth. The ablation depth is found from,

$$\Delta m = 2\pi r L \rho \Delta x, \tag{5.4}$$

assuming uniform mass loss in all radial directions for the entire length of the sleeve. Equating the two expressions for the heat flux allows for the temperature to be solved for directly as:

$$T = \left[\frac{(\Delta x)\rho H_{sub}}{f\sigma_s} \right]^{1/4}, \tag{5.5}$$

which results in the approximate average temperatures seen in Table 5.1.

As with the temperatures calculated from spectroscopic measurements, the average temperatures remain essentially constant for shots of approximately the same input energy. Only shot S782, at 3.7kJ, had significantly less input energy, and the resulting average temperature is less than the other two aluminum shots calculated.

The estimated temperatures are higher than those calculated from the neutral copper lines. This could be a result of the model approximating the average temperature inside the capillary, whereas the temperatures were all measured outside of the source. Another source of difference between the measurements and estimates is the 10% fraction for the incident blackbody radiation. Also, though the measured temperatures were essentially the same for all materials, the estimated temperature differ

Table 5.1: Average temperature estimations for aluminum, copper, and Lexan.

	Aluminum	Copper	Lexan
σ_s (W/m^2K^4)	$5.671(10)^{-8}$	$5.671(10)^{-8}$	$5.671(10)^{-8}$
f_{vs}	0.1	0.1	0.1
ρ (kg/m^3)	2700	8960	1180
H_{sub} (J/kg)	111930000	5732000	59400000
r (m)	$1.985(10)^{-4}$	$1.985(10)^{-4}$	$1.985(10)^{-4}$
L (m)	0.060	0.060	0.119
Δm (kg)	$5.307(10)^{-4}$ (S781)	$4.142(10)^{-4}$ (S790)	$5.385(10)^{-5}$ (S784)
	$5.307(10)^{-4}$ (S782)	$5.2(10)^{-4}$ (S805)	$5.3(10)^{-5}$ (S798)
	$6.434(10)^{-4}$ (S785)		
Δx (m)	$2.627(10)^{-3}$	$6.178(10)^{-4}$	$3.075(10)^{-4}$
	$1.750(10)^{-3}$	$7.755(10)^{-4}$	$3.026(10)^{-4}$
	$3.184(10)^{-3}$		
T_{avg} (K)	11052.2	8648.8	7851.7
	9984.6	9154.8	7820.6
	11596.9		
T_{avg} (eV)	0.95	0.75	0.68
	0.86	0.79	0.67
	1.00		

between materials. Still, most important to notice is that all of the temperatures can be considered low, thus confirming the first assumption about ET plasmas.

5.2 Average Density Calculations

The model of the average plasma density is based on the conductivity of a partially ionized plasma determining the heat input to the plasma from [4]:

$$\sigma = \frac{n_e e^2}{m_e(\bar{\nu}_{en} + \bar{\nu}_{ei})}, \tag{5.6}$$

where σ is the plasma conductivity, n_e is the electron density, $\bar{\nu}_{en}$ and $\bar{\nu}_{ei}$ are the average electron-neutral and electron-ion collision frequencies respectively.

The first approximations made in this model deal with the collision frequencies. Based on [37] and [4], the electron-neutral collision frequency is found from:

$$\bar{\nu}_{en} = n_n \bar{Q}_{en} \sqrt{\frac{8k_B T}{\pi m_e}}, \tag{5.7}$$

where n_n is the neutral particle density, $\bar{Q}_{en}$ is the average electron-neutral collision cross-section, k_B is Boltzmann's constant, T is the plasma temperature, and m_e is the mass of an electron. The electron-ion

collision frequency can be found from:

$$\bar{\nu}_{ei} = \frac{38 Z_{eff} n_e e^2 ln(1 + 1.4\Lambda_m^2)^{1/2}}{\gamma_e m_e T^{3/2}}, \tag{5.8}$$

where Z_{eff} is the effective ion charge, Λ_m is the modified Coulomb parameter, and γ_m is the nonideality parameter. The above expression for the average electron-ion collision frequency includes an approximation for the Coulomb parameter. However, for the low-temperature range of interest in this work, this approximation is very inaccurate. In [38], the percent relative error between the estimation and the analytical solution was found to be as high as 100%. In addition, the SIRENS electrothermal plasma typically has a very low ionization fraction, and therefore is dominated by neutrals. So, the electron-ion collisions will be neglected and the conductivity approximated as:

$$\sigma = \frac{n_e e^2}{m_e \bar{\nu}_{en}}. \tag{5.9}$$

One of the largest assumptions made to calculate the density estimates is in the calculation of the average electron-neutral collision frequency. The neutral particle density is calculated from the fractional sleeve mass lost. This mass loss is assumed to consist only of the material of interest. However, this is not actually the case. The ablated material is composed of mass from the cathode, the material of interest, and the small Lexan piece in the case of the segmented sleeves. For the Lexan shots, there is cathode material in addition to Lexan. With this assumption stated explicitly, the neutral particle density is approximated as:

$$n_n = \frac{\rho N_A}{MW} * \frac{\Delta m}{m_0}, \tag{5.10}$$

where ρ is the material density, N_A is Avogadro's number, MW is the molecular weight, Δm is the sleeve mass loss, and m_0 is the original sleeve mass.

Continuing with the average electron-neutral collision frequency approximation, the average collision cross-section is approximated using a hard-sphere collision model. So that the cross-section is calculated from:

$$\bar{Q}_{en} = \pi R^2 = \pi (R_0 A^{1/3})^2 = \pi (1.2(10)^{-15} * A^{1/3})^2, \tag{5.11}$$

where A is the atomic mass number for the particle of interest: copper, aluminum, and Lexan ($C_{16}H_{14}O_3$).

The final approximation needed to directly calculate the plasma electron density from this model is the plasma conductivity. The plasma conductivity is approximated from the plasma resistivity, which is calculated from the measured current and voltage. As seen in Figure 5, the plasma is purely resistive when the current is initiated, which is for the approximately 100μsec of the current pulse. The conductivity is therefore calculated as:

$$\sigma = \frac{1}{\eta} = \frac{L}{RA}, \tag{5.12}$$

where the resistance is calculated from the measured current and voltage, A is the cross-sectional area of the capillary, and L is the length of the sleeve of interest.

Using the equations discussed above, the estimated densities for aluminum, copper, and Lexan plasmas are seen in Table 5.2. Evident in the results of Table 5.2 is that the estimated neutral particle densities for each material are significantly larger than the estimated electron densities. The seven orders of magnitude difference between these densities confirms the initial assumption that the plasma is dominated by neutrals.

The estimated electron densities are also less than experimentally determined densities. The difference could be due to the neglecting the electron-ion contribution. Or, the difference could be due to any combination of the approximations used with the original model. Still, what is important to notice about the estimated densities is that they are relatively high. The aluminum and copper densities definitely confirm the ET plasma assumption of a high density plasma. The Lexan densities are lower, but still large enough.

5.3 Average Pressure Calculations

The equation of state for the plasma can be used to compare the measured pressure with the pressure calculated with the average density and temperature estimates. Based on the neutral versus electron density results from the previous section, the plasma pressure is estimated from:

$$P = n_e k_B T + n_i k_B T + n_n k_B T = 2 n_e k_B T + n_n k_B T, \tag{5.13}$$

where the total pressure is the sum of the electron, ion, and flow pressures. The estimated total pressures are presented in Table 5.3. The higher aluminum and copper temperatures and densities resulted in much higher pressures than the peak pressures measured by the pressure transducer. The Lexan estimated pressures are much lower than the peak pressures measured experimentally – as expected from the lower densities. Also important to note is that the electron densities make a negligible contribution to the total pressure.

Table 5.2: Average density calculations for aluminum, copper, and Lexan.

	Aluminum	Copper	Lexan
e^2 (C^2)	$2.566(10)^{-38}$	$2.566(10)^{-38}$	$2.566(10)^{-38}$
m_e (kg)	$9.11(10)^{-31}$	$9.11(10)^{-31}$	$9.11(10)^{-31}$
k (J/K)	$1.38(10)^{-23}$	$1.38(10)^{-23}$	$1.38(10)^{-23}$
R (Ω)	0.01	0.02	0.1
ρ ($\Omega * m$)	$1.25(10)^{-5}$	$2.99(10)^{-5}$	$1.25(10)^{-4}$
σ_{dc} ($1/\Omega * m$)	80178.8	$8.42(10)^{7}$	25188.9
N_A (mol^{-1})	$6.023(10)^{-23}$	$6.023(10)^{-23}$	$6.023(10)^{-23}$
MW (kg/mol)	0.027	.063546	.25429
ρ (km/m^3)	2700	8960	1180
n_n (m^{-3})	$6.02(10)^{28}$	$8.49(10)^{28}$	$2.79(10)^{27}$
r (m)	$1.985(10)^{-4}$	$1.985(10)^{-4}$	$1.985(10)^{-4}$
L (m)	0.06	0.06	0.119
Δm (kg)	$5.307(10)^{-4}$ (S781)	$4.142(10)^{-4}$ (S790)	$5.385(10)^{-5}$ (S784)
	$3.535(10)^{-4}$ (S782)	$5.20(10)^{-4}$ (S805)	$5.30(10)^{-5}$ (S798)
	$6.434(10)^{-4}$ (S785)		
fractional mass loss	0.12	0.028	0.010
	0.079	0.037	0.010
	0.14		
n_n in plume (m^{-3})	$7.177(10)^{27}$	$2.396(10)^{27}$	$2.789(10)^{25}$
	$4.778(10)^{27}$	$3.099(10)^{27}$	$2.750(10)^{25}$
	$8.681(10)^{27}$		
T_{avg} (K)	11052.	11686.	12590.
	9985.	12370.	12540.
	11597.		
v_{th} (m/s)	$6.53(10)^{5}$	$6.71(10)^{5}$	$6.97(10)^{5}$
	$6.21(10)^{5}$	$6.91(10)^{5}$	$6.96(10)^{5}$
	$6.69(10)^{5}$		
$\bar{Q}_{en}$ (m^2)	$3.970(10)^{-29}$	$7.163(10)^{-29}$	$2.46(10)^{-29}$
$\bar{\nu}_{en}$ (s^{-1})	$1.861(10)^{5}$	$1.152(10)^{5}$	478.2
	$1.177(10)^{5}$	$1.533(10)^{5}$	470.5
	$2.305(10)^{5}$		
n_e (m^{-3})	$3.20(10)^{20}$	$9.91(10)^{20}$	$1.63(10)^{17}$
	$2.03(10)^{20}$	$1.32(10)^{21}$	$1.61(10)^{17}$
	$3.97(10)^{20}$		

Table 5.3: Average estimated pressure calculations for aluminum, copper, and Lexan.

	Aluminum	Copper	Lexan
T (K)	11052	11686	12590
	9985	12370	12540
	11597		
n_e (m^{-3})	$3.20(10)^{20}$	$9.91(10)^{20}$	$1.63(10)^{17}$
	$2.03(10)^{20}$	$1.32(10)^{21}$	$1.61(10)^{17}$
	$3.97(10)^{20}$		
n_n (m^{-3})	$7.18(10)^{27}$	$2.40(10)^{27}$	$2.79(10)^{25}$
	$4.78(10)^{27}$	$3.10(10)^{27}$	$2.75(10)^{25}$
	$8.68(10)^{27}$		
P (MPa)	$1.09(10)^{3}$	386.	4.85
	658.	529.	4.76
	$1.39(10)^{3}$		

Chapter 6

Conclusions

With metal and insulator capillaries, particulate was generated on the micron size scale and smaller. Current, voltage, pressure, and mass loss measurements were made for almost every shot as well as a series of optical emission spectroscopic measurements, taken for the main materials used.

6.1 Particulate Generation and Characterization

The metal vapor plasmas consistently produced significant amounts of particulate that were clearly visible on a variety of substrates including metal and fabric buttons. The plasma from insulators sleeves produced less particulate that was visible on fabric surfaces, but not on metallic substrates. Also, the composition of the nonmetallic particles could not be completely determined due to similar elements contained in both the particulate and the substrate. Some of the particulate was apparently composed of cathode material.

Comparing the sizes of particulate from different materials, the aluminum particulate was larger than the copper particulate. This result agrees with the particulate measured in [8], even though those shots were taken at slightly lower input energies. Otherwise, the mass ablated and the particles sizes were comparable.

In general, there appears to be a slightly increasing trend in the particulate size with the distance from the source. Figure 6.1, shows this trend best for the largest particles in each image, and somewhat less for the middle-sized particles. However, it does appear that the smallest size of the particulate is basically constant. This trend could relate to the agglomeration of particulate; the smaller the particle, the less agglomeration takes place and the larger particles agglomerate more. As a comparison, Fig. 6.2 shows less of an increasing trend due to the large particles at the second distance from the source exit. The smallest sized particles again remain almost constant.

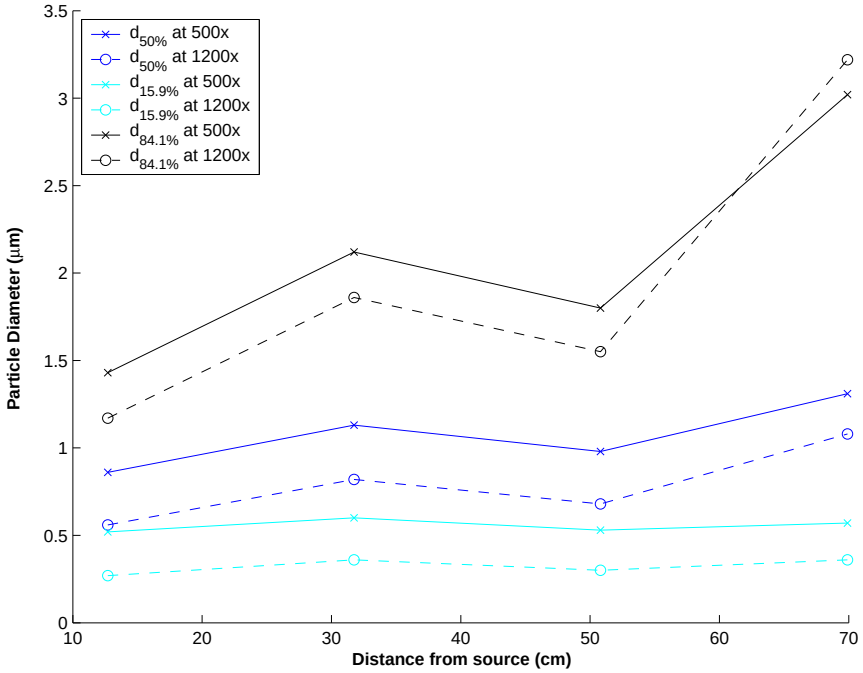

Figure 6.1: Comparison of particle sizes from Al shot S781 with distance from source

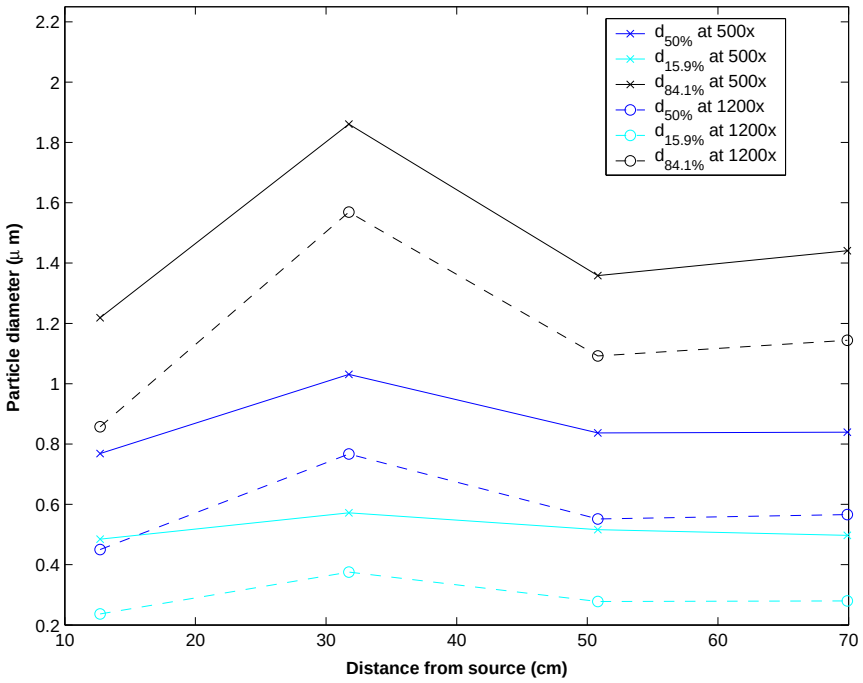

Figure 6.2: Comparison of particle sizes from Al/Cu shot S789 with distance from source

6.2 Optical Emission Spectroscopy

6.2.1 Plasma Temperature

The temperatures calculated by the relative method using neutral copper lines showed a constant trend over the length of the chamber and consistency between liner materials. These shots were all taken at approximately the same input energy, so perhaps the temperature is more strongly dependent on input energy than on liner material. In the one case when the neutral copper lines could not be used, the singly ionized aluminum lines resulted in a significantly higher temperature at the location closest to the source. It seems more likely that this temperature is a result of the uncertainty in the calculation rather than in an actual difference in the temperature of the aluminum plasma close to the source.

Due to the large number of lines present in each spectrum, it was difficult to find enough individual lines from one species to generate a reasonable Boltzmann plot. Using different species to calculate the temperature would be useful to confirm the LTE condition. However, the difference between the temperatures found using aluminum and copper lines in an aluminum plasma was not all that great considering the large uncertainty in the data. The source of the statistical weights and energy levels can also make a large difference in the temperature calculated. The data from [34] leads to higher temperatures from copper lines than the data presented, which was from [35].

Additionally, relative line intensities from the same element and ionization state do not necessarily give an accurate temperature. Besides the large amount of uncertainty in the statistical weights, the differences between the upper energy levels is relatively small. Having a small separation, on the order of the thermal energies, makes the relative method less sensitive to temperature. There is a relative method that uses intensities from different ionization states, but it requires knowledge or estimation of the electron density and a fairly large electron density [22]. An independent measurement of the density, such as from a Langmuir probe, is needed to use this alternate method.

The temperatures presented in [13] for the similar ET device PIPE are a good confirmation for the 0.5eV temperatures determined in this work. The temperatures in [13] were measured at distances two to four inches from the barrel exit and ranged from 0.5eV to 0.73eV. In SIRENS, the temperatures were measured over a much larger distance from the source and at higher input energies; the input energies used in [13] were 4.0kJ. Also good to notice from the other study is that that temperatures were determined to be constant, within the uncertainty, both axially and radially. Therefore, the temperatures should not need to be determined radially in SIRENS.

In the study [19], the input energies used were higher (5-7kJ), and the temperatures measured from the neutral copper lines were significantly higher - around 2eV. However, some of these temperatures were obtained using Boltzmann plots with only 2 points, so the temperatures calculated are much less certain. Also investigated in [19] was temperature as a function of input energy; an increasing trend was observed. This trend needs further investigation when considering that equivalent temperatures were

found at 4kJ in [13] and at 5.7-5.8kJ in this work.

6.2.2 Plasma Density

In most cases, the densities calculated using the Stark broadening of either the Hα or Cu I lines show decreasing trends with distance from the source exit. In figures 6.3 and 6.4, these trends can be seen. These figures include the $\pm$30% error estimated for both analysis methods. Included in Fig. 6.3 are power fits to the aluminum and Lexan densities. The copper density does not appear to follow the same decreasing trend. This could be due to material differences. Aluminum has a much lower melting temperature than copper.

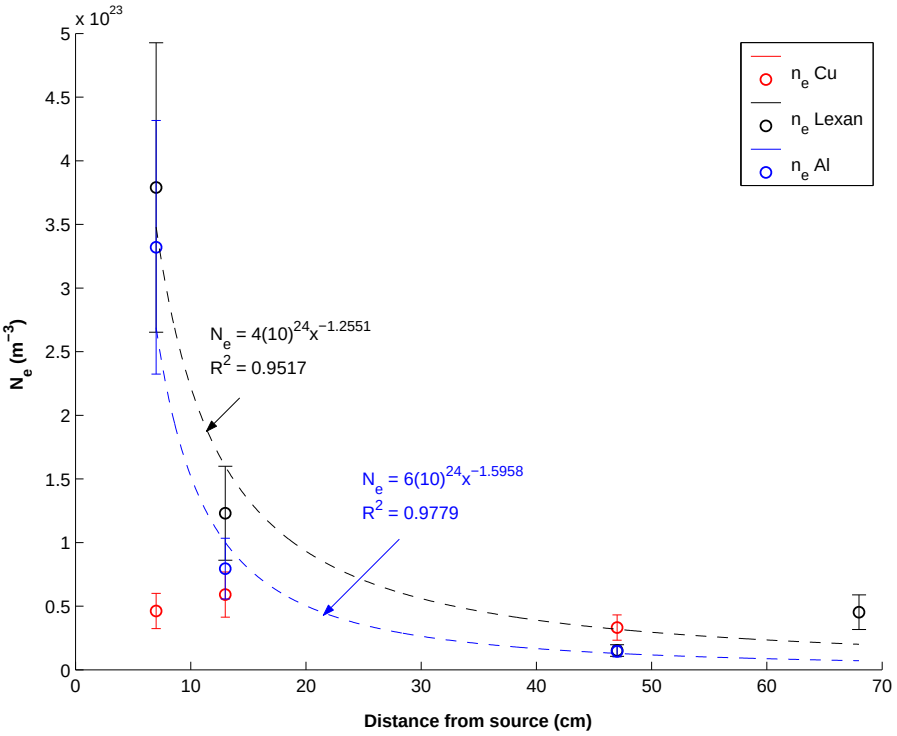

Figure 6.3: Comparison of densities calculated from Stark broadening of Hα line with distance from source.

A decreasing trend in density versus distance is expected due to recombination in the plasma as it expands out from the source. This expectation is confirmed in the figures of the spectra presented in Chapter 3. The background blackbody shape decreases in each type of plasma until it appears almost constant at the farthest location. The evolution of the plasma with distance from the source corresponds to the beginning of departure from LTE. The lines broaden more as the plasma expands, but the plasma does not lose much thermal energy - as seen in the constant temperature. The significant recombination that takes place as the plasma expands means that the plasma transitions to a neutral gas form [33]. However, the evolution signals only the beginning of LTE departure, the plasma can still be considered

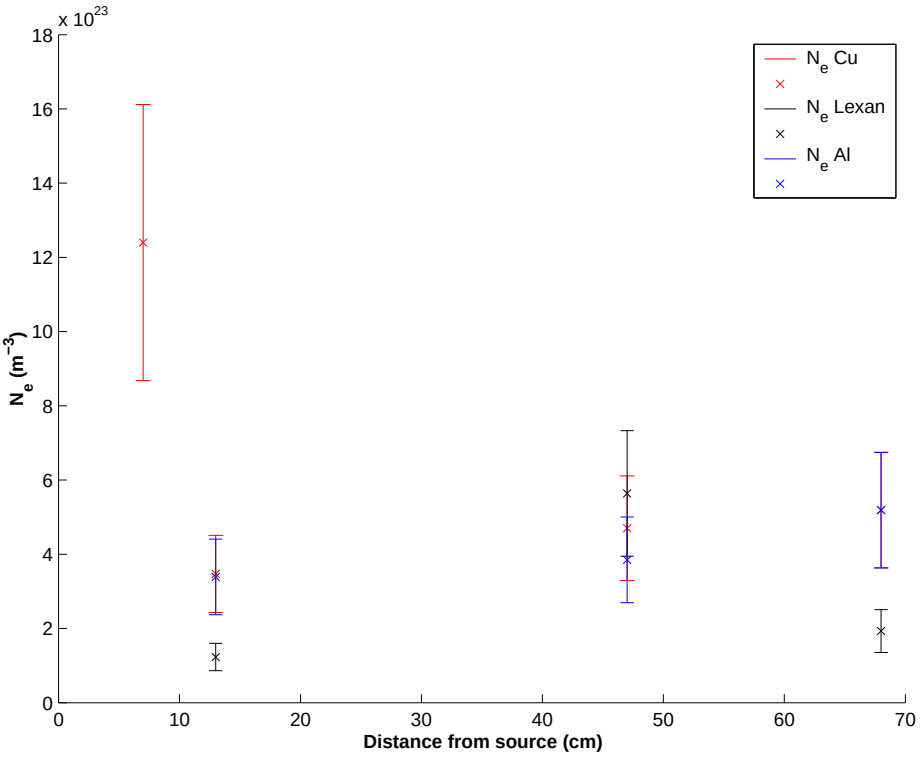

Figure 6.4: Comparison of densities calculated from Stark broadening of Cu I lines with distance from source

at LTE. This assumption is necessary for the spectroscopic measurements to be valid at each of the positions.

6.3 Plasma Parameters

The temperatures estimated based on the radiative heat flux model are generally somewhat higher than the temperatures calculated from the neutral copper lines. However, the estimated temperatures compare closely with the temperature calculated from singly ionized aluminum lines. Also, the estimated Lexan temperatures are within the error of the measured temperature. Since the estimated plasma temperature is an average value at the plasma source, it is not surprising that the temperature would be lower outside the source. This could be one explanation for the difference; the approximations and assumptions about the conductivity and black-body model could also be explanations. For instance, the conductivity might not be constant over the length of the pulse. Or, the fraction of the black-body radiation blocked could be different from the 10% estimated, and could change over the course of the discharge.

The electron densities estimated from the conductivity are several orders of magnitude less than the densities found from spectroscopy. The assumptions made, such as neglecting electron-ion collisions and approximating the neutral density, could be responsible for the difference. In addition, the estimation

is an average taken at the source. Each of the spectroscopic measurements was outside the source. It is expected that the density inside the capillary would be different than outside. A combination of these assumptions is mostly likely responsible for this underestimation.

Though the estimated parameters confirm the needed assumptions about the plasma, it can be useful to further compare the values estimated from the plasma parameter scaling with measured parameters. As in the plasma parameter scaling, the total pressures were calculated using the plasma equation of state for several shots for which temperature and density measurements were obtained. While both the electron and neutral densities were used to calculate the pressure, it was seen that the measured or estimated electron densities had a negligible effect of the total pressure when the neutral density was taken from the fraction of mass ablated.

Based on [13], the static pressure measurements with the pressure transducer should be measuring the total pressure. The change in the local dynamic pressure is negligible because the transducer does not perturb the flow out of the barrel. However, the pressures calculated from the equation of state, in Table 6.1, differ from the measured pressures by an order of magnitude. The pressures calculated from the measured quantities are similar to the estimated quantities.

Each of the temperature and density calculations brings uncertainty to the pressure calculation. In addition, the transducer showed some damage over time, but the consistency of the measurements discounted this as a major error factor. Another very likely error source is electrical noise. The piezoelectric transducers are very sensitive to the electromagnetic noise generated by the pulsed ET discharge. In the past, the noise was apparent in the observed pulses. Well-insulated cables were used to transmit the signal from the transducers to the charge amplifiers, which were kept in the shielded control room. As in [13], well-insulated cables were used in the present work, but the charge amplifiers were not kept in the additionally shielded box. The observed pulses did not display the noisy characteristics seen in the past. The pulses behaved nicely, lagging the current pulse slightly as expected. Still, some or all of the measured pulses could be artifacts of the discharge.

Finally, the pressure transducers were never successfully calibrated. Calibration would indicate if there was drift in the crystal. A change of 1.5V measured could result in an extra 150MPa of pressure. Such an offset could explain the order of magnitude difference between measured and expected values. Calibration was attempted with the shock tube from [13] was used, but reliable results could not be obtained. One major problem with attempted calibration is that it should be in the expected range of experimental measurements. It is not possible to obtain pressures that high with the shock tube available [33].

The main purpose of the parameter estimates is not to compare with measured values, but to help prove the assumptions necessary for the calculation of the important parameters from measurements. In this regard, the estimates show a low temperature, high density plasma which is dominated by neutrals.

Table 6.1: Average pressure calculations for aluminum, copper, and Lexan from measured temperatures and densities.

	Aluminum	Copper	Lexan
T (K)	5800	5800	5800
n_e (m^{-3})	$3.32(10)^{23}$ (S799)	$4.62(10)^{22}$ (S800)	$3.79(10)^{23}$ (S798)
	$7.95(10)^{22}$ (S802)	$5.91(10)^{22}$ (S801)	
	$1.45(10)^{22}$ (S806)	$3.32(10)^{22}$ (S805)	
n_n (m^{-3})	$9.76(10)^{27}$	$2.55(10)^{27}$	$2.76(10)^{25}$
	$1.12(10)^{28}$	$2.15(10)^{27}$	
	$4.94(10)^{27}$	$3.08(10)^{27}$	
P (MPa)	781.	204.	2.27
	900.	172.	
	395.	246	
P_{meas} (MPa)	77.22		49.64
	66.19	71.71	
	66.19	66.19	

Chapter 7

Future Work

7.1 Particulate Generation and Characterization

As mentioned in the Introduction, only one template, or pattern transfer, test was performed. This test was not completely successful, due to the destruction of portions of the pattern and fabric. However, there are many possible tests that could be performed using different placements of the pattern with respect to the fabric, different pattern materials, and/or different fabrics. Washing tests of pattern transfers is also very important, because the durability of the implanted material is vital.

Depending on the specific application, different materials such as graphite could be studied, and different substrate materials could be used. Of particular interest with Lexan capillaries is to find a button substrate upon which the particles would "stick" so that more accurate size distributions could be developed. In addition, backfilling the chamber with a gas, such as nitrogen, is of interest to determine if mixed composition particulate could be generated. A gas such as fluorine could potentially be used to avoid the difficulty of Teflon sleeves.

To optimize the size of particles generated, the input energy needs to be varied. It is expected that increased energy input would result in smaller particulate. Verification of this hypothesis, as well as the size distribution axially for different energy inputs would be useful. Generating particulate on the nanometer size scale is of great interest. The particulate generated in the present work was on average, approximately a micron in diameter. For particulate to be classified as nano-sized, the diameter must be limited to approximately 100nm in diameter. This size range was met in only a small percentage of the particulate measured. In addition to generating particles, entraining these particles into filaments or other nano-sized structures is of great interest.

In general, more images from SEM need to be acquired and analyzed to guarantee that statistically significant particles sizes are returned from the distributions.

7.2 Plasma Characterization

To gain an independent verification of the plasma parameters, Langmuir probe measurements would be ideal. If the electrical noise issues could be resolved, then axial measurement with a single probe would be a good comparison with the temperatures and densities calculated via optical spectroscopy.

Langmuir probe measurements would also help determine where the plasma recombination takes place axially. The evolution of the plasma emission spectra indicates that processes such as recombination are taking place as the plasma plume expands down the length of the chamber. Using biased buttons, effectively single probes, could determine how this process occurs, and could potentially lead to controlling the species deposited on a material of interest.

To verify the pressure measurements, calibrated pressure transducers need to be used at the barrel exit. Taking static and dynamic pressure measurements at different locations axially could also help confirm the densities and temperatures determined from OES.

Bibliography

[1] O E Hankins and M A Bourham. Observations of visible light emission from interaction between an electrothermal plasma and a propellant. *IEEE Transactions on Magnetics*, 33(1):295 – 298, January 1997.

[2] J P Sharpe, B J Merrill, D A Petti, M A Bourham, and J G Gilligan. Modeling of particulate production in the sirens plasma disruption simulator. *Journal of Nuclear Materials*, 2000.

[3] S Shengyi, Z Shikui, and S Chengwei. Discharge of the plasma generator in electrothermal-chemical launchers. *IEEE Transactions on Magnetics*, 33(1):328 – 333, January 1997.

[4] L L Raja, P L Varghese, and D E Wilson. Modeling of the electrothermal ignitor metal vapor plasma for electrothermal-chemical guns. *IEEE Transactions on Magnetics*, 33(1):316 – 321, January 1997.

[5] J D Hurley, M A Bourham, and J G Gilligan. Numerical simulation and experiment of plasma flow in the electrothermal launcher sirens. *IEEE Transaction on Magnetics*, 1998.

[6] M A Bourham, O E Hankins, O Auciello, J M Stock, B W Wehring, R B Mohanti, and J G Gilligan. Vapor shielding and erosion of surfaces exposed to a high heat load in an electrothermal accelerator. *IEEE Transaction on Plasma Science*, 17(3):386 – 391, June 1989.

[7] D Zoler and R Alimi. A proof of the need for consistent treatment in modelling of capillary ablative discharges. *J. Phys. D.: Appl. Phys.*, 28:1141 – 1152, 1995.

[8] J. P. Sharpe. *Particulate Generation During Disruption Simulation on the SIRENS High Heat Flux Facility*. PhD thesis, North Carolina State University, 1996.

[9] D. Zoler, Z. Kaplan, and J. Ashkenazy. Analysis of powder particle accerleration and heating processes in a discharge capillary-ablative pipe device. *Plasma Sources Sci. Technol.*, 5:588–601, 1996.

[10] J U Kim and Y Ko. Electrothermal-chemical synthesis of nanocrystalline aluminum nitride using a metal vapor pulsed plasma jet. *IEEE Transactions on Plasma Science*, 29(4):649 – 652, August 2001.

[11] O.E. Hankins, M.A. Bourham, J. Earnhart, and J.G. Gilligan. Visible light emission measurements from a dense electrothermal launcher plasma. *IEEE Transactions on Magnetics*, 29(1):1158–1161, January 1993. 1.

[12] O.E. Hankins and David Mann. Analyses of molecular and neutral atomic emission spectra from an electrothermal launcher plasma. *IEEE Transactions on Magnetics*, 31(1):410–413, January 1995.

[13] Christopher Hobbs. Temporal and spatial characterization of freely expanding electrothermal plasma jet. Master's thesis, North Carolina State University, 2000.

[14] Kohel. Pulsed plasma jet. *IEEE Trans. Magnetics*, 1999.

[15] Travis K. Gray. Plasma source flow and performance in a coaxial source with an enhanced pulse forming network. Master's thesis, North Carolina State University, 2001.

[16] www.pearsonelectronics.com.

[17] Kistler Instrument Corp. data sheet. 217c and 617c ballistics pressure sensors.

[18] www.kistler.com.

[19] K Murali. Plasma optical spectroscopy. Master's thesis, North Carolina State University, 1999.

[20] S.M. Bennet and H.R. Griem. Technical report #71-097. Technical report, Center for Theoretical Physics of the Department of Physics, University of Maryland, College Park, MD, 1971.

[21] H.K. Forsen. Plasma spectroscopy. January 1968.

[22] H. Griem. *Plasma Spectroscopy.* McGraw-Hill, 1 edition, 1964.

[23] X Zhou, Y Li, J Wang, and Z Huang. The temperature measurement of the electrothermal-chemical launcher plasma by atomic emission spectroscopy. *IEEE Transactions on Plasma Science*, 29(2):360 – 364, April 2001.

[24] W. L. Wiese, D. E. Kelleher, and D. R. Paquette. Detailed study of the stark broadening of balmer lines in a high-density plasma. *Physical Review A*, 6(3):1132–1153, September 1972.

[25] H. Griem. *Spectral Line Broadening by Plasmas.* Academic Press, 1 edition, 1974.

[26] Dipak H. Oza, Ronald L. Greene, and Daniel E. Kelleher. Collisional broadening of the balmer-α transition of h and he^+ in plasmas. *Physical Review A*, 37(2):531–536, January 1988.

[27] Marco A. Gigosos and Valentín Carde noso. New plasma diagnosis tables of hydrogen stark broadening including ion dynamics. *J. Phys. B: At. Mol. Opt. Phys.*, 29:4795–4838, 1996.

[28] J M Luque, M D Calzada, and M Saez. Experimental reseach into the influence of ion dynamics when measuring the electron density from the stark broadening of the h_α and h_β lines. *J. Phys. B: At. Mol. Opt. Phys.*, 36:1573–1584, April 2003.

[29] P. Kepple and H. R. Griem. Improved stark profile calculations for the hydrogen hα, hβ, hγ, and hδ. *Physical Review*, 173:317–325, 1968.

[30] J U Kim and H Suk. Characterization of a high-density plasma produced by electrothermal capillary discharge. *Applied Physics Letters*, 80(3):368 – 370, January 2002.

[31] J.T. Knudtson, W.B. Green, and D.G. Sutton. The uv-visible spectroscopy of laser-produced aluminum plasmas. *J. Appl. Phys.*, 61(10):4771–4780, May 1987.

[32] *AATCC Technical Manual*, 1994.

[33] Mohamed Bourham. Personal Communication.

[34] *CRC Handbook of Chemistry and Physics*. CRC Press, Boca Raton, FL, 76th edition, 1996.

[35] J. Reader, C. H. Corliss, W. L. Wiese, and G. A. Martin. *Wavelengths and Transition Probabilities for Atoms and Atomic Ions*, volume NSRDS-NBS 68 of *National Standard Reference Data System*. National Bureau of Standards, December 1980.

[36] M R Zaghloul, M A Bourham, and J M Doster. Semi-analytical modelling and simulation of the evolution and flow of ohmically-heated non-ideal plasmas in electrothermal guns. *J. Phys. D: Appl. Phys.*, 34:772 – 786, 2001.

[37] R J Zollwig and R W Liebermann. Electrical conductivity of nonideal plasmas. *J. Appl. Phys.*, 62(9):3621 – 3627, November 1987.

[38] M.R. Zaghloul, M.B. Bourham, J.M. Doster, and J.D. Powell. On the average electron-ion momentum transport cross-section in ideal and non-ideal plasmas. *Physics Letters A*, 262(1):86–89, October 1999.

Appendix A

Complete Shot Summary

Table 1: Complete Shot Summary

Shot No.	Liner Material	Net E (kJ)	Peak I (kA)	Peak V (kV)	Peak P (MPa)	Notes
780	Lexan/Al fuse	2.636	-	-	-	particulate collected
781	Maycor/Al/Lexan	5.725	-	-	-	particulate collected
782	Maycor/Al/Lexan	3.690	-	-	-	particulate collected
783	Lexan	5.594	41.8	−5.12	-	diagnostic shot
784	Lexan	5.616	43.2	−5.12	44.1	particulate collected
785	Maycor/Al/Lexan	5.725	-	-	-	-
786	Teflon	5.714	-	-	-	particulate collected
787	Teflon	5.748	44.6	−4.08	-	diagnostic shot
788	Maycor/Cu/Lexan	5.822	66.2	−3.7	88.3	particulate collected
789	Maycor/Cu,Al/Lexan	5.836	-	-	66.2	particulate collected
790	Maycor/Cu/Lexan	5.838	-	-	-	Langmuir probe test shot
791	Maycor/Cu,Al/Lexan	5.831	65.5	-5.28	71.7	particulate collected; endplate pattern transfer
792	Lexan	5.685	-	-	49.6	spectrometer test shot, triggering wrong
793	Lexan	5.551	-	-	-	spectrometer test shot, triggering wrong
794	Lexan	5.697	41.8	-2.28	49.6	spectrometer test shot, need attenuation

Table 1: continued

Shot No.	Liner Material	Net E (kJ)	Peak I (kA)	Peak V (kV)	Peak P (MPa)	Notes
795	Lexan	5.625	-	-	55.2	spectrometer test shot, triggering wrong
796	Lexan	5.685	30.2	−4.72	55.2	spectrometer with hardware triggering, need attenuation
797	Lexan	5.702	-	-	-	spectra clipped
798	Lexan	5.722	43.2	−5.52	49.6	spectra obtained
799	Maycor/Al/Lexan	5.833	74.2	−2.8	77.2	spectra obtained
800	Maycor/Cu/Lexan	5.822	76.3	−3.2	-	spectra obtained, too much attenuation
801	Maycor/Cu/Lexan	5.833	73.4	−6.72	71.7	spectra obtained, 2nd position
802	Maycor/Al/Lexan	5.840	70.6	−5.04	66.2	spectra obtained, 2nd position
803	Lexan	5.675	41.0	−4.32	49.6	spectra obtained, 2nd position
804	Lexan	5.694	42.5	−5.76	44.1	spectra obtained, 3rd position
805	Maycor/Cu/Lexan	5.838	69.8	−2.96	66.2	spectra obtained, 3rd position
806	Maycor/Al/Lexan	5.836	71.3	−3.78	66.2	spectra obtained, 3rd position
807	Lexan	5.691	43.2	−5.92	77.2	spectra obtained, 4th position
808	Maycor/Al/Lexan	5.840	80.6	−6.72	60.7	spectra obtained, 4th position
809	Maycor/Cu/Lexan	5.840	70.6	−5.6	55.2	spectra obtained, 4th position
810	Lexan	5.669	40.3	−3.6	38.6	spectra obtained, 3rd position redo

Appendix B

Full Particle Sizing Data Summary

Table 2: Particle size analysis data summary.

Image	Magnification	Scale (pixel/μm)	Area (μm^2)	min d (μm)	# of particles
781b115x	500x	2.13	45052.78935	0.5297555	1768
781b125x	500x	2.13	45052.78935	0.5297555	1149
781b135x	500x	2.13	45052.78935	0.5297555	470
781b145x	500x	2.13	45052.78935	0.532254	600
781b1112x	1200x	5.1	7858.515955	0.0223441	115
781b1212x	1200x	5.1	7858.515955	0.221251	338
781b1312x	1200x	5.1	7858.515955	0.223441	376
781b1412x	1200x	5.1	7858.515955	0.2256758	223
781b1130x	3000x	12.7	1267.282535	0.088849	51
781b1230x	3000x	12.7	1267.282535	0.088155	88
781b1330x	3000x	12.7	1267.282535	0.088849	67
781b1430x	3000x	12.7	1267.282535	0.0125651	41
781b415x	500x	2.13	45052.78935	0.529755477	544
781b425x	500x	2.13	45052.78935	0.532254324	270
781b4112x	1200x	5.1	7858.515955	0.223441414	107
781b4212x	1200x	5.1	7858.515955	0.223441414	94
781b4130x	3000x	12.7	1267.282535	0.089553932	30
781b4230x	3000x	12.7	1267.282535	0.088848736	35
781b515x	500x	2.13	45052.78935	0.529755	379
781b525x	500x	2.13	45052.78935	0.52728	1639
781b535x	500x	2.13	45052.78935	0.532254	343
781b545x	500x	2.13	45052.78935	0.529755	545

Table 2: continued

Image	Magnification	Scale (pixel/μm)	Area (μm^2)	min d (μm)	# of particles
781b5112x	1200x	5.1	7858.515955	0.221251	158
781b5212x	1200x	5.1	7858.515955	0.223441	190
781b5312x	1200x	5.1	7858.515955	0.223441	168
781b5412x	1200x	5.1	7858.515955	0.223441	144
781b5130x	3000x	12.7	1267.282535	0.088849	26
781b5230x	3000x	12.7	1267.282535	0.088849	30
781b5330x	3000x	12.7	1267.282535	0.088849	46
781b5430x	3000x	12.7	1267.282535	0.088849	34
781b815x	500x	2.13	45052.78935	0.529755477	97
781b825x	500x	2.13	45052.78935	0.529755477	37
781b8112x	1200x	5.1	7858.515955	0.223441414	26
781b8212x	1200x	5.1	7858.515955	0.223441414	30
789b15x	500x	2.13	45052.78935	0.22041482	180
789b35x	500x	2.13	45052.78935	0.22041482	1129
789b55x	500x	2.13	45052.78935	0.22041482	1635
789b75x	500x	2.13	45052.78935	0.22041482	130
789b85x	500x	2.13	45052.78935	0.22041482	1206
789b95x	500x	2.13	45052.78935	0.22041482	578
789b105x	500x	2.13	45052.78935	0.22041482	935
789b125x	500x	2.13	45052.78935	2.20414821	865
789b112	1200x	5.05	8014.9005	0.03921184	221
789b312	1200x	5.05	8014.9005	0.07842368	445
789b512	1200x	5.05	8014.9005	0.03921184	84
789b712	1200x	5.05	8014.9005	0.03921184	317
789b812	1200x	5.05	8014.9005	0.03921184	648
789b912	1200x	5.05	8014.9005	0.03921184	162
789b1012	1200x	5.05	8014.9005	0.03921184	388
789b1212	1200x	5.05	8014.9005	0.03921184	460
789b130x	3000x	12.7	1267.282535	0.00620001	125
789b330x	3000x	12.7	1267.282535	0.00620001	58
789b530x	3000x	12.7	1267.282535	0.00620001	210
789b730x	3000x	12.7	1267.282535	0.00620001	62
789b830x	3000x	12.7	1267.282535	0.00620001	135

Table 2: continued

Image	Magnification	Scale (pixel/μm)	Area (μm^2)	min d (μm)	# of particles
789b930x	3000x	12.7	1267.282535	0.00620001	82
789b1030x	3000x	12.7	1267.282535	0.00620001	78
789b1230x	3000x	12.7	1267.282535	0.0062001	137
b2,3	-	7.55	3585.80764	0.149454193	604
b2,4	-	6.4	4990.234375	0.176309236	612
b3,1	3000x	12.6	1287.477954	0.089553932	238
b3,2	3000x	12.7	1267.282535	0.088848736	173
b5,1	-	16.9	715.6612163	0.066768017	273
b6,1	-	1.7	70726.6436	0.66375245	865
b6,2	-	6.3	5149.911817	0.179107793	111
782,2,1	300x	1.33	115552.038	0.848405387	275
782,2,2	800x	3.52	16496.64256	0.320562254	116
782,2,4	2500x	11	1689.256198	0.102579907	40
782,2,5	350x	1.55	85078.0437	0.727986559	301
782,2,6	4000x	17.4	675.122209	0.064849414	149
782,3,2	900x	3.98	12903.71455	0.283512356	24
782,3,3	2000x	8.8	2639.46281	0.12822489	11
782,4,1	120x	0.532	722200.2374	2.121013471	561
782,4,2	350x	1.55	85078.0437	0.727986559	149
782,8, 1	200x	0.88	263946.281	1.282249052	122
782,8,2	180x	0.796	322592.8638	1.417561766	141
782,17,1	700x	3.08	21546.63518	0.366256879	107
782,17,2	3000x	13.2	1173.094582	0.085483268	40
782,17,3	2500x	11	1689.256198	0.102579907	30
782,17,4	1000x	4.4	10557.85124	0.256449804	63
782,17,5	350x	1.55	85078.0437	0.727986559	381
784,4,2	3500x	15.5	850.780437	0.072798648	20
784,4,5	3500x	15.5	850.780437	0.072798648	47
784,6,2	2000x	8.8	2639.46281	0.12822489	53
784,9,2	800x	3.5	16685.71429	0.322394042	74
u5	-	4.28	11158.17975	0.26363991	32

Appendix C

Experimental Density Calculations

The data presented in this appendix summarizes the results from the different methods initially used to calculate the plasma electron density.

The method used in [27] resulted in the values reported for the H_α broadening. Several other methods, based on [22] and [25] were also attempted. For the first method from [22], the densities were calculated based on the simple expression for Stark broadening of the H_α line:

$$N_e = C(N_e, T)\Delta\lambda_S^{3/2}, \tag{1}$$

where $C(N_e, T)$ is a coefficient that depends only slightly on electron density and temperature and $\Delta\lambda_S$ is the measured FWHM. Values for the coefficient were taken at T=10,000K and either $N_e = 10^{16}$ or $N_e = 10^{17}$ cm^{-3} from the table in [22].

The second method, from [25], involves the calculation of the reduced wavelength α as,

$$\alpha = |\Delta\lambda|/2.6eN^{2/3}. \tag{2}$$

The reduced wavelength was calculated for several orders of electron density magnitude. Using the tables in [25], the electron density was then interpolated using the calculated values for α.

The final method from [27] was well explained in Chapter 2, and densities were calculated for both 5000K and 10,000K temperatures. There was so little difference between the two temperatures that it was not necessary to interpolate to obtain accurate densities at the calculated 5800K temperature. The temperatures reported in the results were taken at 5000K.

For the density calculations using the neutral copper lines, the Stark widths were taken from the data tables assuming, a temperature of 10,000K and a density of 10^{17}. Then using the Stark width, w_m and the FWHM determined for each line, the density was found from the ratio of the widths as:

$$N_e = \frac{FWHM_{true}}{w_m} * 10^{23} \quad m^{-3}. \tag{3}$$

For each shot where copper lines were fit, the density was taken as the average of the densities calculated for each visible line.

All wavelength and FWHM measurements are presented in nm and all densities have units of m^{-3}. The instrumental broadening was taken after each shot when the fiber or attenuator conditions changed. However, these changes affected the broadening very little, and averaged to the 0.3nm seen in both tables.

The most noticeable feature of each method is the decreasing trend in the density. This trend corresponds to the density decreasing with axial distance from the source. In addition, there is only a very slight dependence on temperature, as expected.

Table 3: H_α Data and Calculation Summary

Species	Shot No.	λ obs.	FWHM obs.	FWHM inst.	FWHM true	α (5000K,N=10^{17})	N_e ([22])	$\log(N_e)$ ([25])	$\log(N_e)$ [27], 5000K	$\log(N_e)$ [27], 10000K
H_α	798	656.281	2.5928	0.3	2.28614	$2.12(10)^{-2}$	$3.95(10)^{23}$	23.58	23.579	23.486
H_α	799	656.348	2.4145	0.3	2.10785	$1.96(10)^{-2}$	$3.49(10)^{23}$	23.18	23.521	23.4296
H_α	800	656.449	0.8862	0.3	0.62925	$5.84(10)^{-3}$	$9.72(10)^{22}$	20.26	22.665	22.5886
H_α	801	656.370	0.9883	0.3	0.73132	$6.79(10)^{-3}$	$1.22(10)^{23}$	20.44	22.771	22.693
H_α	801	656.376	1.1290	0.3	0.87707	$8.14(10)^{-3}$	$9.38(10)^{22}$	20.70	22.900	22.819
H_α	803	656.407	1.4001	0.3	1.14816	$1.07(10)^{-2}$	$1.40(10)^{23}$	21.19	23.091	23.007
H_α	805	656.467	0.7659	0.3	0.51395	$4.77(10)^{-3}$	$7.18(10)^{22}$	20.06	22.523	22.447
H_α	806	656.400	0.6452	0.3	0.30852	$2.86(10)^{-3}$	$3.34(10)^{22}$	19.69	22.160	22.092
H_α	807	656.440	0.6549	0.3	0.31817	$2.95(10)^{-3}$	$3.50(10)^{22}$	19.71	22.182	22.114
H_α	810	656.421	0.9216	0.3	0.62163	-	$9.55(10)^{22}$	-	22.656	22.580

Table 4: Copper Data and Calculation Summary

Species	Shot	λ obs.	w_m $\mathring{A}$	FWHM$_{meas}$ (nm)	FWHM$_{true}$ ($\mathring{A}$)	N_e	Avg. N_e
Cu I	800	510.554	0.43	0.8331688	5.331688	$1.23993(10)^{24}$	$1.24(10)^{24}$
Cu I	801	510.554	0.43	0.62355035	3.2355035	$7.52443(10)^{23}$	$3.47(10)^{23}$
Cu I	801	578.213	0.72	0.5017484	2.017484	$2.80206(10)^{23}$	
Cu I	801	515.324	1.9	0.62799768	3.2799768	$1.7263(10)^{23}$	
Cu I	801	522.007	2.2	0.69802703	3.9802703	$1.80921(10)^{23}$	
Cu I	802	510.554	0.43	0.60965232	3.0965232	$7.20122(10)^{23}$	$3.39(10)^{23}$
Cu I	802	578.213	0.72	0.45371798	1.5371798	$2.13497(10)^{23}$	
Cu I	802	515.324	1.9	0.67748685	3.7748685	$1.98677(10)^{23}$	
CuI	802	522.007	2.2	0.79527342	4.9527342	$2.25124(10)^{23}$	
Cu I	803	522.007	2.2	0.57139975	2.7139975	$1.23364(10)^{23}$	$1.23(10)^{23}$
Cu I	805	510.554	0.43	0.71059063	4.1059063	$9.54862(10)^{23}$	$4.70(10)^{23}$
Cu I	805	578.213	0.72	0.5233037	2.233037	$3.10144(10)^{23}$	
Cu I	805	515.324	1.9	0.72309938	4.2309938	$2.22684(10)^{23}$	
Cu I	805	522.007	2.2	1.16146551	8.6146551	$3.91575(10)^{23}$	
Cu I	806	510.554	0.43	0.6659345	3.659345	$8.5101(10)^{23}$	$3.85(10)^{23}$
Cu I	806	578.213	0.72	0.41046654	1.1046654	$1.53426(10)^{23}$	
Cu I	806	522.007	2.2	0.63281589	3.3281589	$1.5128(10)^{23}$	
Cu I	807	578.213	0.72	0.43907939	1.3907939	$1.93166(10)^{23}$	$1.93(10)^{23}$
Cu I	808	510.554	0.43	1.41903243	11.1903243	$2.6024(10)^{24}$	$1.65(10)^{24}$
Cu I	808	522.007	2.2	1.832842	15.32842	$6.96746(10)^{23}$	
Cu I	809	510.554	0.43	0.79746988	4.9746988	$1.15691(10)^{24}$	$5.19(10)^{23}$
Cu I	809	578.213	0.72	0.75290827	4.5290827	$6.29039(10)^{23}$	
Cu I	809	515.324	1.9	0.3909262	0.909262	$4.78559(10)^{22}$	
Cu I	809	522.007	2.2	0.83373146	5.3373146	$2.42605(10)^{23}$	
Cu I	810	510.554	0.43	0.8331688	5.331688	$1.23993(10)^{24}$	$5.64(10)^{23}$
Cu I	810	578.213	0.72	0.49706961	1.9706961	$2.73708(10)^{23}$	
Cu I	810	522.007	2.2	0.69001579	3.9001579	$1.7728(10)^{23}$	